

AD-A136 132

DEVELOPMENT AND APPLICATIONS OF THE MICROCHANNEL  
SPATIAL LIGHT MODULATOR(U) MASSACHUSETTS INST OF TECH  
CAMBRIDGE DEPT OF ELECTRICAL ENGIN. C WARDE 30 JUN 83  
AFOSR-TR-83-1107 AFOSR-77-3328 F/G 20/5

1/1

UNCLASSIFIED

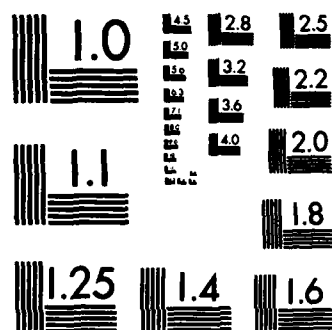
NL

END

FILMED

144

DTIC



MICROCOPY RESOLUTION TEST CHART  
NATIONAL BUREAU OF STANDARDS-1963-A

AD-A136 132

DEVELOPMENT AND APPLICATIONS OF THE  
MICROCHANNEL SPATIAL LIGHT MODULATOR

FINAL  
~~AFOSR-77-3328~~ REPORT, AFOSR-77-3328

June 30, 1983

Cardinal Warde

Department of Electrical Engineering  
and Computer Science

Massachusetts Institute of Technology  
Cambridge, Massachusetts 02139, USA

DTIC  
DEC 20 1983  
H J D

Approved for public release

Distribution unlimited

DTIC FILE COPY

AIR FORCE OFFICE OF SCIENTIFIC RESEARCH

Bolling Air Force Base, D.C. 20332

Approved for public release;  
distribution unlimited.

83 12 20 033

DEVELOPMENT AND APPLICATIONS OF THE  
MICROCHANNEL SPATIAL LIGHT MODULATOR

FINAL  
~~INTERIM~~ REPORT, AFOSR-77-3328


June 30, 1983

Cardinal Warde

Department of Electrical Engineering  
and Computer Science

Massachusetts Institute of Technology  
Cambridge, Massachusetts 02139, USA

Approved for public release  
Distribution unlimited

Accession For	
NTIS GRA&I	<input checked="checked" type="checkbox"/>
DTIC TAB	<input type="checkbox"/>
Unannounced	<input type="checkbox"/>
Justification	
By	
Distribution/	
Availability Codes	
Dist	Avail and/or Special
A1	

AIR FORCE OFFICE OF SCIENTIFIC RESEARCH  
Bolling Air Force Base, D.C. 20332

AIR FORCE OFFICE OF SCIENTIFIC RESEARCH (AFSC)  
NOTICE OF TRANSMITTAL TO DTIC  
This technical report has been reviewed and is  
approved for public release IAW AFR 190-12.  
Distribution is unlimited.  
MATTHEW J. KERPER  
Chief, Technical Information Division



REPORT DOCUMENTATION PAGE		READ INSTRUCTIONS BEFORE COMPLETING FORM
1. REPORT NUMBER <b>AFOSR-TR- 83-1107</b>	2. GOVT ACCESSION NO. <b>AD-A136132</b>	3. RECIPIENT'S CATALOG NUMBER
4. TITLE (and Subtitle)  <b>DEVELOPMENT AND APPLICATIONS OF THE MICROCHANNEL SPATIAL LIGHT MODULATOR</b>		5. TYPE OF REPORT & PERIOD COVERED <b>FINAL <del>Interim</del> Report</b> <b>Sept. 30, 1981 - Dec. 31, 1982</b>
		6. PERFORMING ORG. REPORT NUMBER
7. AUTHOR(s)  <b>Cardinal Warde</b>		8. CONTRACT OR GRANT NUMBER(s)  <b>AFOSR-77-3328</b>
9. PERFORMING ORGANIZATION NAME AND ADDRESS <b>Room 13-3134, Dept of Electrical Engineering Massachusetts Institute of Technology 77 Massachusetts Avenue, Cambridge, MA 02139</b>		10. PROGRAM ELEMENT, PROJECT, TASK AREA & WORK UNIT NUMBERS  <b>61102F 2305/B2</b>
11. CONTROLLING OFFICE NAME AND ADDRESS <b>Air Force Office of Scientific Research/NE Bolling Air Force Base, D.C. 20332 Dr. John Neff</b>		12. REPORT DATE <b>JUN 30, 83</b>
		13. NUMBER OF PAGES <b>68</b>
14. MONITORING AGENCY NAME & ADDRESS (if different from Controlling Office)		15. SECURITY CLASS. (of this report)  <b>unclassified</b>
		15a. DECLASSIFICATION/DOWNGRADING SCHEDULE
16. DISTRIBUTION STATEMENT (of this Report)  <div style="text-align: center;">Approved for public release; distribution unlimited. ✓</div>		
17. DISTRIBUTION STATEMENT (of the abstract entered in Block 20, if different from Report)		
18. SUPPLEMENTARY NOTES <b>Portions published in Optics Letters, 3, 196, 1978; Applied Optics, 20, 2066, 1981. Opt. Eng., 20, 1, 1981; Optics Letters, 7, 344, 1982; Optics Letters, 8, 353, 1983.</b>		
19. KEY WORDS (Continue on reverse side if necessary and identify by block number)  <b>Spatial Light Modulator, Incoherent-to-coherent image transducer, Real-time optical information processing, Optical logic, Image processing, Adaptive optics.</b>		
20. ABSTRACT (Continue on reverse side if necessary and identify by block number) <b>The Microchannel Spatial Light Modulator (MSLM) is a versatile, highly sensitive, and optically-addressed device that is well suited for low-light-level, real time, optical information processing. The image processing operations that can be achieved with the MSLM include contrast reversal, contrast enhancement, edge enhancement, image addition and subtraction, analog and digital intensity level thresholding, and binary-level logic operations such as AND, OR, EXCLUSIVE OR, XOR, NAND and NOR. Several of these operations are demonstrated herein. Recent prototype MSLMs have exhibited a half-wave exposure of 2 nJ/cm<sup>2</sup>, an optical</b>		

unclassified

SECURITY CLASSIFICATION OF THIS PAGE(When Data Entered) -3-

information storage time of more than two months, and a framing rate of 40 Hz with full modulation depth (200 Hz with 20% modulation depth). The theoretical details of operation of the device are described in the Applied Optics paper which constitutes Appendix I of this report. Recent advances in crystal polishing techniques have resulted in the availability of thin, high quality  $\text{LiNbO}_3$  crystals, and in a concomitant increase in the spatial resolution and the optical quality of the device. Spatial resolutions of better than 2 cycles/mm at 50% contrast ( $\sim 10$  cycles/mm at 10% contrast) have been achieved. Additionally, we have shown theoretically and experimentally how the MSLM, functioning as a phase-only modulator, can be successfully integrated into high resolution all optical adaptive systems to perform wavefront phase compensation for applications such as atmospheric optical communication and imaging through randomly fluctuating media.

unclassified

SECURITY CLASSIFICATION OF THIS PAGE(When Data Entered)

# TABLE OF CONTENTS

COVER PAGE -----	1
REPORT DOCUMENTATION PAGE -----	2
LIST OF FIGURES -----	5
PREFACE -----	6
INTRODUCTION -----	7
OPERATIONAL DETAILS -----	9
Electron Accumulation Write mode -----	15
Electron Depletion Write mode -----	17
READOUT MODES -----	19
CYCLING MODES AND OTHER ERASE MECHANISMS -----	21
SPACE-DOMAIN PROCESSING MODE -----	22
Secondary Electron Emission -----	11
WRITE MODES -----	15
Analog Thresholding -----	24
Real-Time Hard Clipping -----	24
Contrast Reversal -----	24
Other Space-Domain Operations -----	26
Limitations of the Space Domain Processing Mode -----	28
MATERIALS LIMITATIONS -----	30
Photocathode -----	30
Microchannel Plate -----	30
Acceleration Grid -----	32
Dielectric Mirror -----	33
Electro-optic Crystal -----	34
Lithium Niobate -----	35
Electro-optic Materials Comparison -----	38
APPLICATIONS TO ADAPTIVE PHASE COMPENSATION -----	40
All-Optical System -----	40
REFERENCES -----	45
COLLABORATION WITH OTHER RESEARCH GROUPS -----	47
PUBLICATIONS RESULTING FROM AFOSR SPONSORSHIP -----	48
LIST OF PERSONNEL -----	50
APPENDICES -----	51
I. C. Warde, et al., Appl.Opt., <u>20</u> , 2066 (1981) -----	51
II. C. Warde and J. Thackara, Opt.Lett., <u>7</u> , 344 (1982) -----	60
III. A. D. Fisher and C. Warde, Opt.Lett., <u>4</u> , 131 (1979) -----	63
IV. A. D. Fisher and C. Warde, Opt.Lett., <u>8</u> , 353 (1983) -----	66

# LIST OF FIGURES

- Fig 1. The Optically Addressed Microchannel Spatial Light Modulator
- Fig 2. Sketch illustrating the dimensions and voltages of the components within the MSLM
- Fig 3. Sketch of the gap current density  $J_g$  in an MSLM as a function of gap voltage  $V_g$  for constant write light intensity and constant MCP bias voltage  $V_b$
- Fig 4. Illustrating the dynamic characteristics of the electron accumulation write mode. (a) After capacitive division of  $V_b$  and before the write light is turned on; (b) electron accumulation with the write light on, and  $V_g$  approaching  $V_{eq}$ ; (c)  $V_b$  being ramped downward while photocathode is flooded with light to achieve erasure by secondary electron emission.
- Fig 5. Illustrating the dynamic characteristics of the electron depletion write mode. (a)  $V_b$  set at  $V_{bb}$  and mirror surface written to equilibrium to give a uniform background; (b)  $V_b$  switched to  $V_{bw}$ , and  $V_g$  approaching  $V_{eq}$  with the write light on; (c)  $V_b$  switched back to  $V_{bb}$  and the image erased by electron accumulation.
- Fig 6. Interferometric readout intensity characteristic as a function of surface charge density for MSLMs with Fabry-Perot crystal etalons with reflectivities of 0.15 and 0.80.
- Fig 7. Graphical illustration of the cross sectional profile of (a) an original image; (b) the image after the MSLM analog thresholding operation; (c) the image after hard clipping; (d) the image after contrast reversal.  $I_T$  is the threshold intensity.
- Fig 8. Some of the open-loop information processing operations that have been achieved by operating the MSLM in its space domain information processing mode.
- Fig 9. Direct-detection phase compensated receiver.
- Fig 10. An all-optical high resolution interference phase loop employing an MSLM.
- Fig 11. Phase compensation results with the all optical IPL/MSLM system.



PREFACE

Development and Applications of the Microchannel Spatial Light Modulator

This final report summarizes the MIT program on the development of the optically-addressed Microchannel Spatial Light Modulator (MSLM). The work was sponsored by the Air Force Office of Scientific Research under Grant No. AFOSR-77-3328.

Since the basic theory of the operation of the MSLM has already been published in open literature, only a brief summary is given in the body of the report. The reader is referred to Appendix I which is a reproduction of the literature on the theory of operation.

→ The fundamental operating characteristics and materials limitations of the device are discussed. The role of secondary electron emission in the operation of the device is stressed and some of the write, cycling, and readout modes and their limitations are described. In addition, the limitations of the inherent space-domain image-processing operations of the device are discussed. In the final section, the report summarizes some of the key results on the application of the MSLM to the problem of high resolution, all-optical, adaptive wavefront phase compensation for communication and imaging through the earth's atmosphere.

## INTRODUCTION

→ The optically-addressed microchannel spatial light modulator (MSLM) is a versatile, real-time optical signal- and image-processing device that exhibits high optical sensitivity and high framing speed. It consists of a photocathode and a microchannel plate (MCP)<sup>1</sup> in proximity focus with an electro-optic crystal plate, as shown in Fig. 1. A planar electron acceleration grid is often placed between the MCP and the electro-optic plate. The electro-optic plate carries a high-resistivity dielectric mirror on one side and a transparent conducting electrode on the other. —————→ S-P<sup>2</sup>

During operation of the MSLM, write light (coherent or incoherent) incident on the photocathode creates an electron image which is amplified by the MCP and proximity focused onto the surface of the dielectric mirror. The resulting surface charge distribution creates a spatially varying electric field that modulates the refractive index of the electrooptic plate. Thus the readout light, which makes a double pass through the crystal, is spatially phase modulated. To erase the image, the surface charge distribution must be erased. A variety of mechanisms for doing so are available, depending on the nature of the charge distribution and the optical, transport and secondary electron emission properties of the surface in which the charge distribution is stored.

The versatility of the MSLM arises from the architecture of the device in which the functions of charge generation, multiplication, transfer, and storage, as well as that of light modulation are performed by separate device components. This design permits independent control of the above processes, allows the device to be tailored for specific applications, and leads to a wide variety of image processing operations that can be achieved by operating the device in its internal, space-domain, image processing mode.

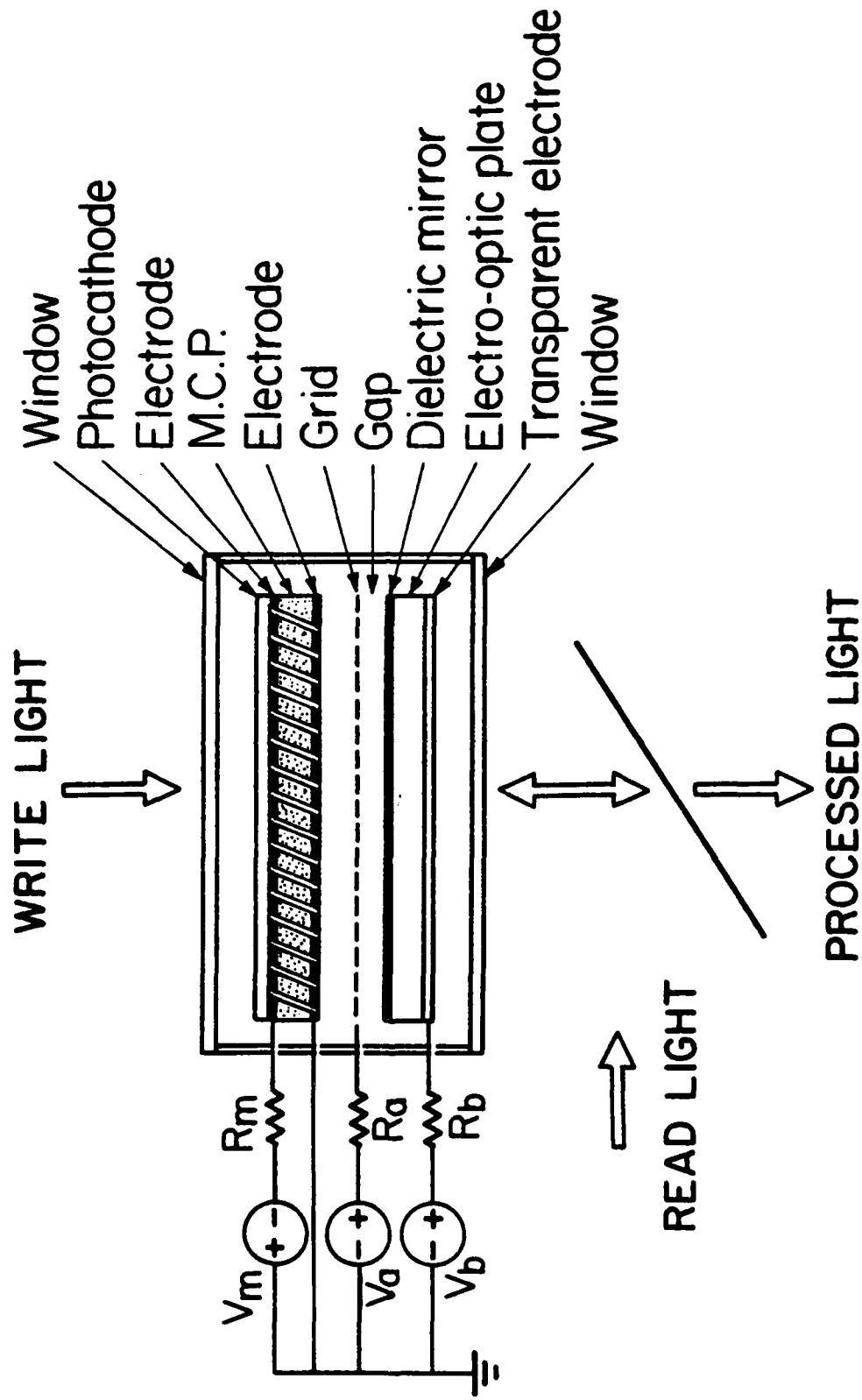


Fig 1. The Optically Addressed Microchannel Spatial Light Modulator

In general, among other applications, spatial light modulators can be used as phase-only modulators, amplitude-only modulators, intensity modulators, Fourier-plane spatial filters, input plane transducers, and space-domain processors. Through proper choice of materials and configurations, the MSLM can be tailored to accomplish any of these functions. This report (1) describes the basic operating modes and principles of the MSLM, (2) illustrates how these relate to some of the important image processing operations that can be achieved when the device is operated as a space-domain processor, (3) discusses how the various materials properties impact on and limit device performance, and (4) explores the application of the MSLM in an all-optical closed-loop, real-time adaptive spatial phase compensation system that could prove useful for communications and imaging through scattering media. Earlier stages of development of the MSLM have been reported in references 2 and 3 (Appendices I and II).

#### OPERATIONAL DETAILS

Figure 2 is a sketch showing the dimensions and voltages of the device components. Under typical biasing conditions, the MCP output electrode is held at ground potential, the grid at  $V_a$  (~2kV) and the crystal electrode at a potential  $V_b$  which is varied during operation. The voltage across the gap between the grid and the crystal surface is  $V_g$  and the voltage across the crystal is  $V_x$ . Thus,

$$V_b = V_a + V_g + V_x, \quad (1)$$

and because the capacitance of the crystal is generally much larger than that of the gap, the changes that are impressed on  $V_b$  during operation are coupled primarily across the gap.

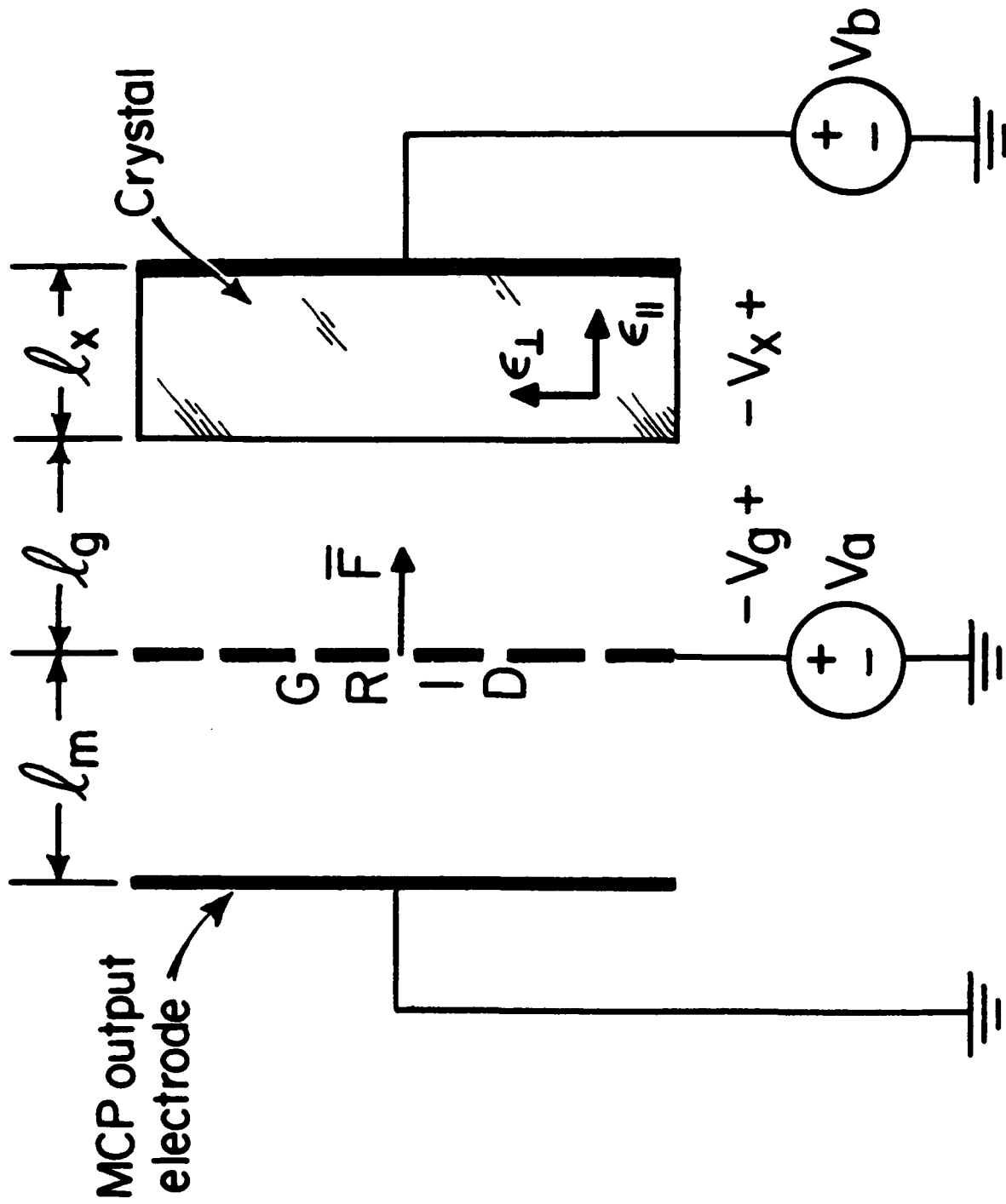


Fig 2. Sketch illustrating the dimensions and voltages of the components within the MSLM

### Secondary Electron Emission

In some MSLMs, the dynamics of the manipulation of the surface charge distribution are determined by the transport and secondary emission properties of the surface in which the charge distribution is stored. In these devices, it is important to note that microchannel plates are not monoenergetic sources of electrons. The output electron current from a typical MCP has a continuous energy distribution  $n_o(V_k)$  that can range between zero and  $eV_m$ , where  $-V_m$  ( $V_m > 0$ ) is the MCP bias voltage, and  $e$  is the electronic charge. The distribution is weighted heavily in favor of the low energy (0 to  $>50\text{eV}$ ) electrons.<sup>4, 5</sup> Here,  $n_o(V_k)dV_k$  is the number of MCP output electrons per unit area per unit time with energy between  $eV_k$  and  $e(V_k + dV_k)$ . The MCP output current density  $J_o$  can therefore be written as

$$J_o = \int_0^{V_m} en_o(I_w, V_k)dV_k \quad (2)$$

In the linear operating regions of the MCP and the photocathode,  $n_o(I_w, V_k)$  scales linearly with the write light intensity  $I_w$ . In terms of the actual device parameters,  $J_o$  can be obtained from the expression

$$J_o = I_w neG/h\nu, \quad (3)$$

where  $n$  is the quantum efficiency of the photocathode,  $G$  is the gain of the MCP,  $h$  is Planck's constant, and  $\nu$  is the frequency of the write light. The primary current  $J_p$  is defined at the surface of the crystal, and in a gridless device  $J_p = J_o$  when none of the MCP electrons is locked out (repelled from the crystal).

In devices employing an acceleration grid, the primary current  $J_p$  is always less than the MCP output current  $J_o$  because the grid intercepts a portion of the MCP output current. If  $n(I_w, V_k, V_a, V_g)$  is the primary electron energy distribution at the surface of the crystal, then

$$J_p = \int_0^{V_m} en(I_w, V_k, V_a, V_g) dV_k \quad (4)$$

Additionally, an effective collected secondary electron emission ratio  $\bar{\delta}'$  may also be defined by

$$\bar{\delta}'(V_m, V_a, V_g) = \frac{1}{J_p} \int_0^{V_m} e\delta'(V_k, V_a, V_g)n(I_w, V_k, V_a, V_g)dV_k \quad (5)$$

where  $\delta'(V_k, V_a, V_g)$  is the ratio of secondary electrons collected by parts of the system other than the crystal to monoenergetic primary electrons with MCP ejection energy  $eV_k$ . Note that  $\bar{\delta}'$  will be greater or smaller than unity depending through Eq.(5) on  $\delta'(V_k, V_a, V_g)$ , the primary electron distribution  $n(I_w, V_k, V_a, V_g)$ , the MCP bias voltage  $-V_m$ , and the crystal bias voltage  $V_b$  which is used to control  $V_g$ . Further details of the secondary electron emission process can be found in Ref.2 (Appendix I).

It is the gap current density  $J_g$  which determines the rates at which electrons accumulate on or are removed from the dielectric mirror surface.  $J_g$  is given by

$$J_g = J_p(1 - \bar{\delta}'). \quad (6)$$

Figure 3 is a sketch of the gap current density  $J_g$  as a function of  $V_g$ , with  $I_w, V_a$  and  $V_m$  constant, for a device employing a grid and operated such that  $V_{eq}$  is positive.

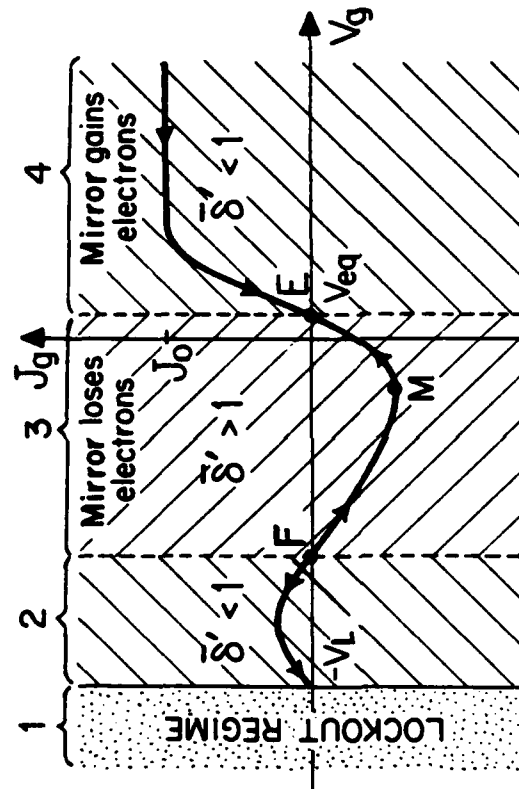


Fig 3. Sketch of the gap current density  $J_g$  in an MSLM as a function of gap voltage  $V_g$  for constant write light intensity and constant MCP bias voltage



Notice that there are four regions of operation in Fig. 3. In region 4, for large positive values of  $V_g$  (achieved with large  $V_b$ ),  $\bar{\delta}'$  is always less than unity because most of the secondary electrons generated are attracted back to the dielectric mirror. In region 3 (the range spanning small positive and small negative values of  $V_g$ ) most of the secondary electrons generated will escape from the dielectric mirror surface and  $\bar{\delta}'$  can be greater than unity. For more negative values of  $V_g$ , there is a region (region 2) in which the energy of the majority of the primary electrons is so low that very few secondary electrons are generated and thus  $\bar{\delta}'$  is again less than unity. Finally, in region 1 ( $(V_g < -V_L)$  where  $V_L = V_a + V_k(\max)$ , and  $eV_k(\max)$  is the ejection energy of the most energetic MCP output electron) all the primary electrons are repelled from the dielectric mirror surface and the gap current is then identically zero. This condition is referred to as lockout.

The point E (corresponding to  $\bar{\delta}' = 1$ ) at the boundary between regions 4 and 3 in Fig. 3 is a stable operating point because (a) in region 4, as electrons accumulate on the mirror,  $V_g$  falls, thereby decreasing the attraction of secondary electrons to the mirror and thus  $\bar{\delta}'$  increases towards unity, and (b) in region 3 as the mirror loses electrons,  $V_g$  increases and attracts a larger fraction of the secondary electrons back to the surface of the mirror, and so  $\bar{\delta}'$  decreases towards unity. By similar arguments, it can be seen that the point F in Fig. 3 is an unstable equilibrium point.

During the standard write and erase processes, the lockout regime is avoided and the device is operated in regions 3 and 4. However, in the space-domain or internal processing mode, sophisticated operations such as multilevel thresholding is achieved by driving certain parts of the image into the lockout regime during operation.

## WRITE MODES

As illustrated in Fig. 3,  $J_g$  may be either positive or negative depending on the operating conditions and, therefore, positive or negative surface charge distributions may be written on the dielectric mirror. Thus two write modes are possible: the electron accumulation mode in which the mirror surface gains the appropriate electron distribution, and the electron depletion (or secondary electron emission) write mode in which an electron distribution is extracted from the surface of the mirror.

### Electron Accumulation Write Mode

In the electron accumulation write mode, which is illustrated in Fig. 4,  $V_b$  initially divides capacitively between the crystal and the gap [Fig. 4(a)] thereby raising  $V_g$  into region 4 of Fig. 3 for which  $\bar{\delta}' < 1$ . Then when the write light is turned on, electrons are deposited on the crystal,  $V_g$  begins to fall toward its equilibrium value  $V_{eq}$ , and the crystal voltage  $V_x$  rises as shown in Fig. 4(b). Electron accumulation may be terminated when the desired  $V_x$  is reached by turning off the write light. To avoid saturation, no parts of the image must be allowed to reach equilibrium. The crystal may be erased via secondary electron emission by flooding the photocathode with light and lowering  $V_g$  (by lowering  $V_b$ ) into region 3 of Fig. 3, where  $\bar{\delta}' > 1$  [see Fig. 4(c)]. In practice, to avoid lockout,  $V_b$  is ramped downward no faster than  $V_g$  is driven to  $V_{eq}$  by the electron removal process.

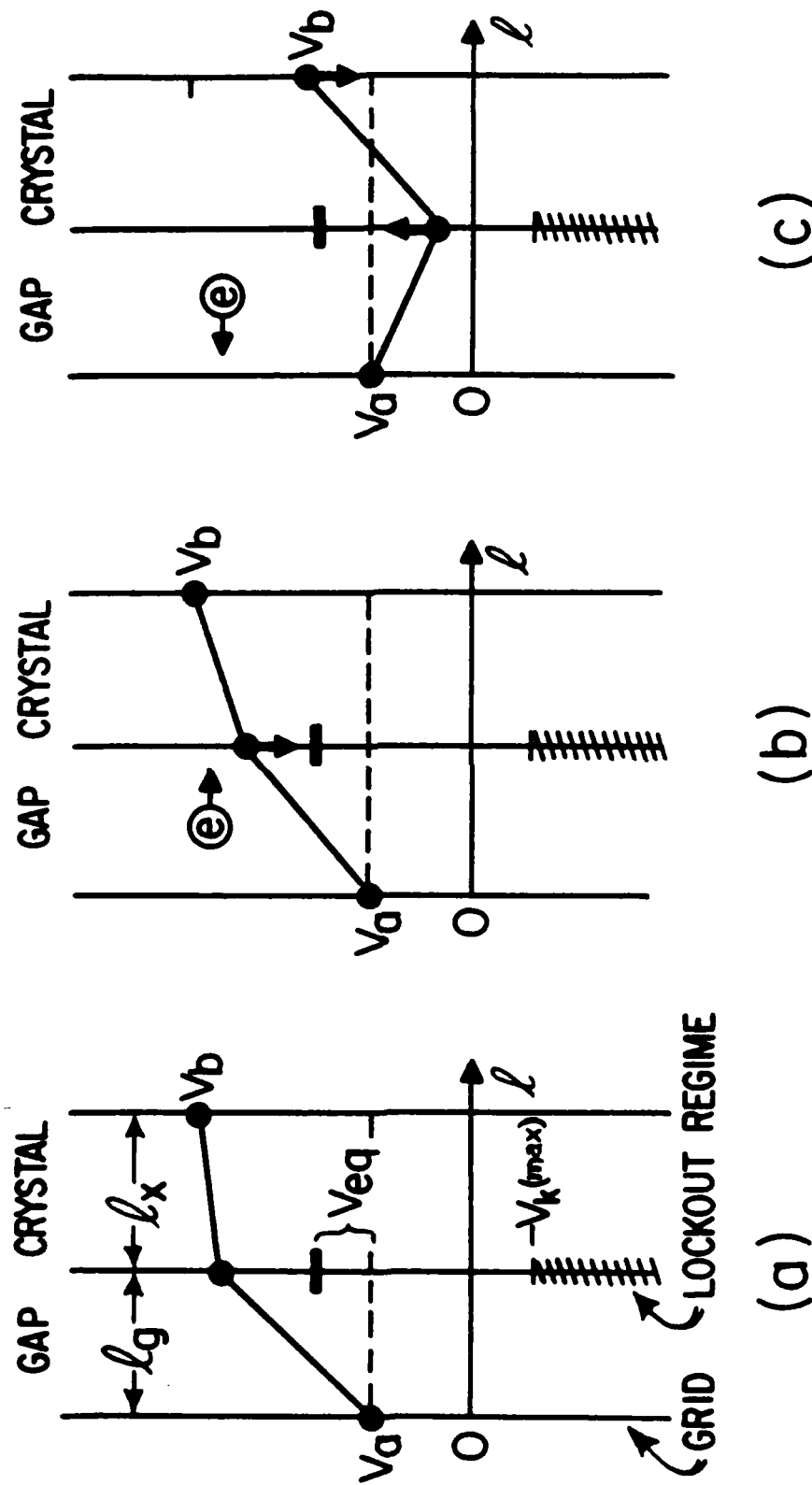


Fig 4. Illustrating the dynamic characteristics of the electron accumulation write mode. (a) After capacitive division of  $V_b$  and before the write light is turned on; (b) electron accumulation with the write light on, and  $V_g$  approaching  $V_{eq}$ ; (c)  $V_b$  being ramped downward while photocathode is flooded with light to achieve erasure by secondary electron emission.

### Electron Depletion Write Mode

In the electron depletion write mode, which is illustrated in Fig. 5, the grid voltage  $V_a$  is set at some positive value which may be several kilovolts depending on the halfwave voltage of the crystal.  $V_b$  is then set at some initial bias level  $V_{bb}$  and the photocathode illuminated uniformly with light so that electrons are deposited or removed from the mirror until all points on the mirror surface are driven to equilibrium and the desired readout background level [see Fig. 5(a)] is obtained.

With the write information incident on the photocathode,  $V_b$  is abruptly switched from the bias value  $V_{bb}$  to the write value  $V_{bw}$ , so that  $V_g$  for all points on the crystal shift into region 3 of Fig. 3 where  $\bar{\delta} > 1$ . Electron removal then begins at a rate which is initially proportional to the write light intensity  $I_w$  [see Fig. 5(b)].

Unfortunately, since  $J_g$  is a function of  $V_g$ , the electron removal rate will not continue to be exactly proportional to  $I_w$  throughout the write process. A more sophisticated control of  $V_b$ , however, can minimize this problem.<sup>6</sup> To erase the image,  $V_x$  can be restored to its original uniform level by again raising  $V_b$  up to  $V_{bb}$  and flooding the photocathode with light [see Fig. 5(c)]. In practice, the value of  $V_a$  is chosen such that  $\Delta V_b$  (where  $\Delta V_b = V_{bb} - V_{bw}$ ) is larger than or equal to the halfwave voltage of the crystal if full modulation depth is desired. Because the device is operated so that no areas of the crystal become locked out, this form of operation is called the non-lockout mode.

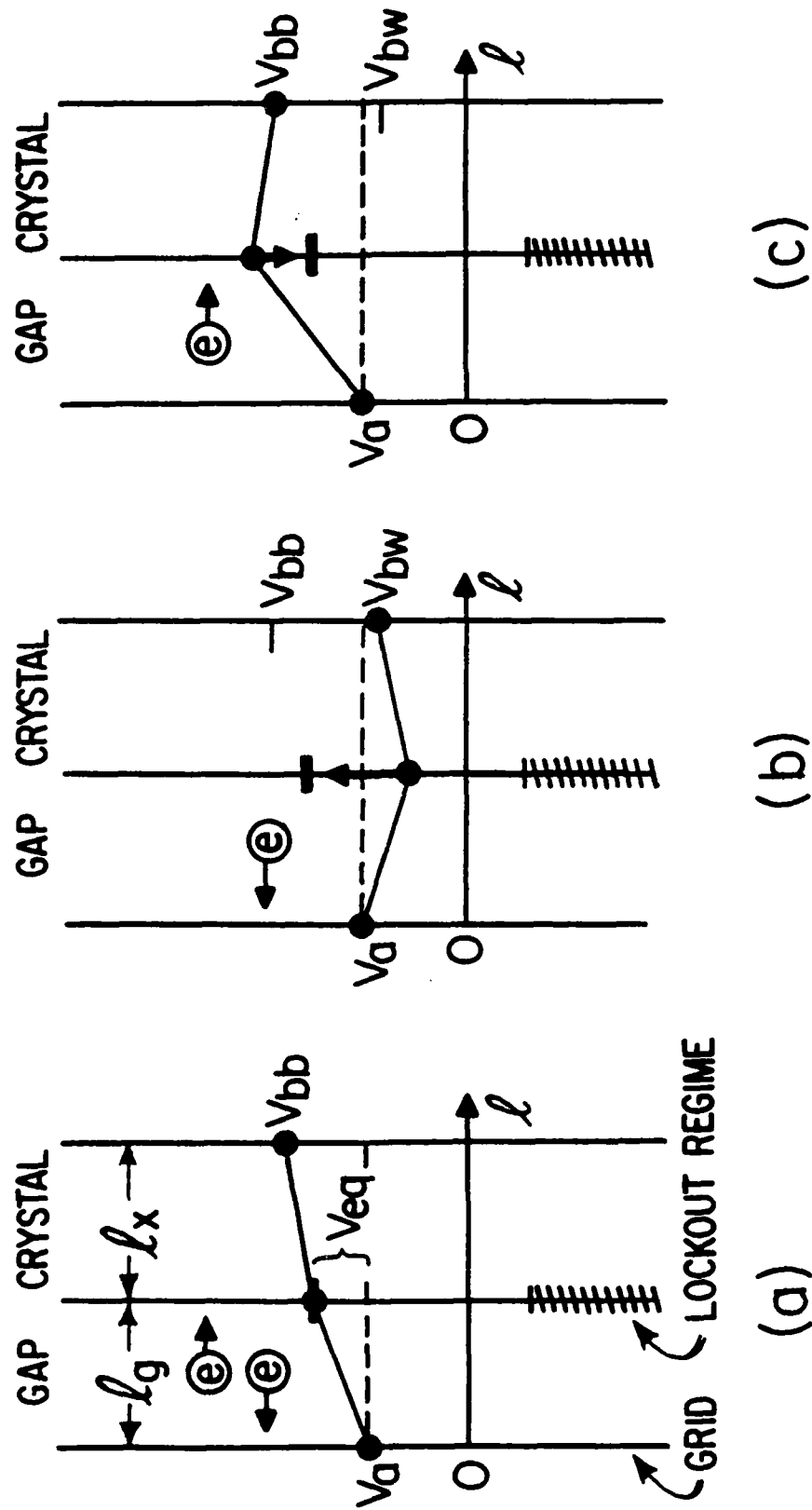


Fig 5. Illustrating the dynamic characteristics of the electron depletion write mode. (a)  $V_b$  set at  $V_{bb}$  and mirror surface written to equilibrium to give a uniform background; (b)  $V_b$  switched to  $V_{bw}$ , and  $V_g$  approaching  $V_{eq}$  with the write light on; (c)  $V_b$  switched back to  $V_{bb}$  and the image erased by electron accumulation.

## READOUT MODES

Optical information that has been written into the MSLM may be read out with crossed polarizers, interferometrically, or with Schlieren optics. The possible readout modes depend on the symmetry and cut of the electrooptic crystal.

For amplitude-only modulation, polarization readout may be used in conjunction with a crystal cut for which the components of the allowed polarizations in the crystal experience phase changes with equal magnitudes but opposite sign. For phase-only modulation, polarization readout may be employed with the polarizer and analyzer oriented along the same induced dielectric axis of the crystal. However, for materials in which the allowed polarization components experience identical phase changes (e.g. in z-cut 3m crystals with longitudinal fields only) it would not be necessary to polarize the readout light. Interferometric and Schlieren readout schemes always lead to simultaneous amplitude and phase modulation (intensity modulation).

The readout mode that was used in the early prototype devices employed the interference between the front and back surface reflections from a plane-parallel electro-optic crystal.<sup>2</sup> If dielectric mirrors are deposited on both sides of such a plane-parallel crystal to form a Fabry-Perot etalon of finesse  $F$ , a complete off-to-on transition can be achieved with approximately  $1/F$  times the halfwave surface charge density of the crystal, and a concomitant increase in framing speed results. The sensitometry of such a device is distinguished by a very large value of gamma, where  $\gamma$  is defined by

$$\gamma = \log(I_{01}/I_{02})/\log(E_2/E_1) \quad (7)$$

Here,  $E_1$  and  $E_2$  and  $I_{01}$  and  $I_{02}$  are the corresponding exposures and readout intensities for two points on the linear portion of the device sensitometry curve. Figure 6 is a plot of the readout intensity vs. surface

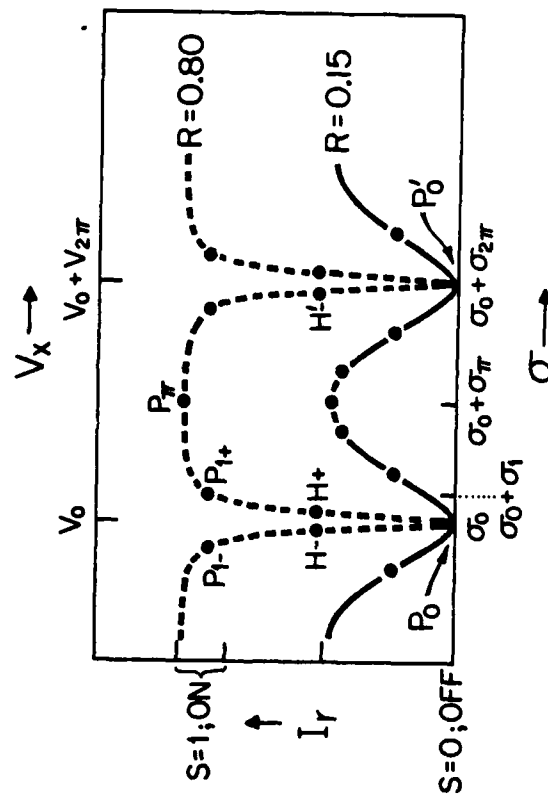


Fig 6. Interferometric readout intensity characteristic as a function of surface charge density for MSLMs with Fabry-Perot crystal etalons with reflectivities of 0.15 and 0.80.

charge density of an MSLM with a Fabry-Perot crystal etalon for two different surface reflectivities.

#### CYCLING MODES AND OTHER ERASE MECHANISMS

The MSLM can be either framed through a discrete sequence of write, read, and erase periods or operated in a continuous mode. In the framed mode, the optical write signal is integrated and stored in the form of a charge distribution on a high resistivity surface; after a readout period of the desired length has elapsed, the charge distribution is removed.

In addition to the erase methods based on electron accumulation and depletion using the MCP and photocathode as the source of electrons, several other erase mechanisms can be employed. For example, high resistivity crystals with high resistivity dielectric mirrors may be coated with an upper layer of photoconductive material which has a high dark resistivity. If a ring electrode is placed on the photoconductor near the edge of this structure, the charge distribution can be removed by flooding the photoconductive layer with light and appropriately biasing the ring electrode.

The continuous mode of operation can be achieved with low resistivity and photoconductive crystals by allowing the charges to bleed through the crystal. In the continuous mode, the instantaneous modulation is proportional to the write image intensity for all temporal variations within the bandwidth of the system. However, large MCP output currents are required to operate the device in the continuous mode, so this mode of operation is not recommended for high framing speed applications.



## SPACE-DOMAIN PROCESSING MODE

By exploiting the secondary-electron-emission characteristics of the dielectric mirror and the charge-readout intensity characteristic of the crystal, the MSLM can be operated in its space-domain information processing mode. In this internal processing mode, the device can perform several sophisticated information processing operations on information that has already been stored in the device and on information as it is being read (in real time) into the device.

The space-domain nonlinear operations of analog thresholding, real-time hardclipping, and contrast reversal are the key to several of the unique space-domain information processing operations that are achievable with the MSLM. These innate operations of the MSLM are a consequence of the secondary electron emission processes that are associated with the electron beam addressing of the floating surface of the dielectric mirror.

Figure 7 is a graphic illustration of the above-mentioned nonlinear operations as they are achieved by the MSLM. By combining these three operations with the standard spatial light modulator operations of (1) multiplication of the write and readout beam intensities, and (2) addition of two or more write beams, plus the fact that multiple  $\pi$  radians of phase retardation are achievable with proper choice of crystal, the MSLM has been able to perform space-domain image subtraction, stored-image hard clipping, real-time and stored-image contrast enhancement, real-time and stored-image edge enhancement, as well as binary-level optical logic operations such as AND, OR, NAND, NOR, XOR and NXOR. The principles and the limitations of the three key operations are described below.

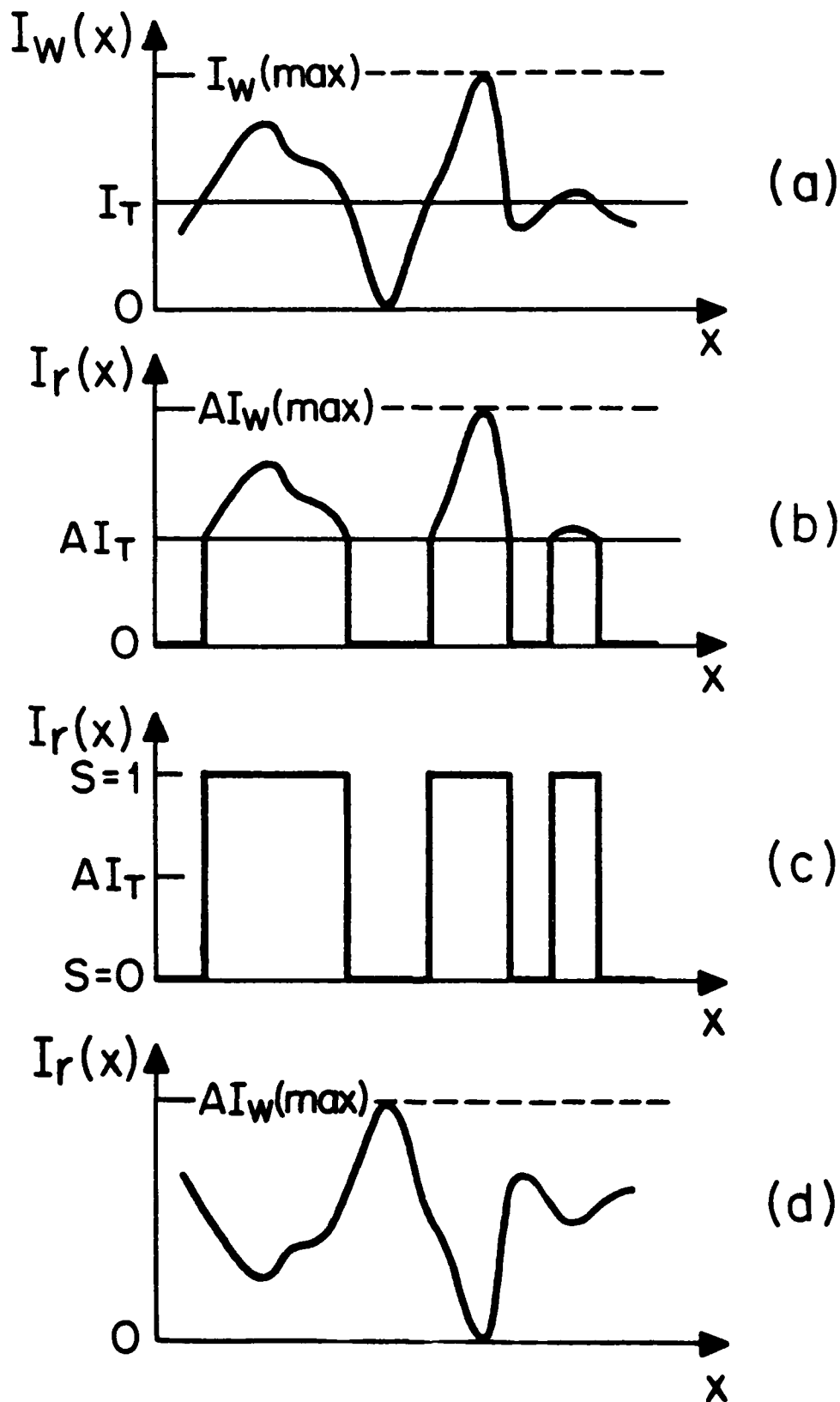


Fig 7. Graphical illustration of the cross sectional profile of (a) an original image; (b) the image after the MSLM analog thresholding operation; (c) the image after hard clipping; (d) the image after contrast reversal.  $I_T$  is the threshold intensity.

### Analog Thresholding

Consider two areas  $A'$  and  $A''$  within an electron distribution on the surface of the crystal with charge densities  $\sigma'$  and  $\sigma''$ , respectively. If  $\sigma''$  is sufficiently greater than  $\sigma'$ , then  $V_b$  can be adjusted so that, when the photocathode is uniformly illuminated, primary electrons from the MCP are repelled from  $A'$  but not from  $A''$ . Under these conditions  $A''$  and all areas with charge densities greater than  $\sigma''$  will be erased, while  $A'$  and all other areas for which  $\sigma < \sigma'$  will be unaffected. This operation (analog level thresholding) corresponds to erasing all the parts of an image for which the intensity falls below some threshold intensity  $I_T$  as illustrated graphically in Fig. 7(b). That is,

$$I_w(x,y) \longrightarrow I_o(x,y) = A[I_{w,max} - I_w(x,y)] \quad (8)$$

where  $I_{w,max}$  is the maximum value of  $I_w(x,y)$ , the write light intensity, and  $A$  is a constant. Repeated applications of this operation (multiple-level thresholding) can be used to analyze the spatial distribution of intensities in an image. Analog thresholding is useful in the implementation of contrast enhancement and the logic operations AND and NAND.

### Real-Time Hard Clipping

This operation is most conveniently performed in the electron depletion (secondary emission) write mode. The MSLM is initially uniformly biased in the OFF state with charge density  $\sigma_0$ . Then  $V_b$  is ramped downward (from higher to lower voltage) at a rate  $\dot{V}_b$  with the optical image incident on the photocathode. All the intensities below some threshold level  $I_T$  (which depends on  $\dot{V}_b$ ) will be barely recorded because, at their locations, electrons cannot be removed fast enough from the crystal to prevent the gap field

from eventually repelling all future primary electrons. Thus, all intensities below threshold will remain at a low intensity level ( $S = 0$  state). Because the slope of the  $V_x$  vs write exposure characteristic can be very steep between threshold and saturation, virtually all write-light intensities above threshold are written to the maximum charge density which is set to coincide with the  $S = 1$  state. The hard-clipping operation is illustrated graphically in Fig. 7(c), where

$$I_w(x,y) \longrightarrow I_o(x,y) = \begin{cases} 1 & I_w(x,y) \geq I_T \\ 0 & I_w(x,y) < I_T \end{cases} \quad (9)$$

This operation can lead to real-time contrast enhancement if the crystal has a low halfwave voltage (e.g. DKDP at  $-51^\circ\text{C}$ ,  $V_\pi < 200\text{V}$ ) and if  $\hat{V}_b$  is adjusted so that the spatial intensity variations of the image are mapped onto the knee of the  $V_x$  vs  $I_w$  curve.<sup>6</sup>

### Contrast Reversal

There are two methods of performing contrast reversal. Since the two write modes permit images to be written as negative or positive charge distributions, pockels-effect-type crystals, because they exhibit the linear electro-optic effect, will yield contrast reversed images when operated in the accumulation and electron depletion write modes. If the image is already stored in the MSLM, then because the readout intensity characteristic is periodic in surface charge density under polarization and interferometric readout, contrast reversal can be achieved by adding the appropriate uniform charge density to dielectric mirror. In this operation,

$$I_w(x,y) \longrightarrow I_o(x,y) = A[I_w(\text{max}) - I_w(x,y)], \quad (10)$$

where  $I_w(\text{max})$  is the maximum value of  $I_w(x,y)$ , the write light intensity, and  $A$  is a constant. This operation is illustrated graphically in Fig. 7(d).

### Other Space-Domain Operations

Figure 8 summarizes some of the results of the space-domain information processing operations achievable with the MSLM.

Figure 8(a) shows the image of an U.S. Air Force resolution chart. The sequence of Figs.8(b)-8(d) illustrates analog and digital space-domain intensity thresholding. Figure 8(b) shows a four-level image. Figure 8(c) shows the same image after space-domain thresholding in which quadrant 1 was reduced to the zero-intensity level of quadrant 3, leaving quadrants 2 and 4 unchanged. Figure 8(d) is the resultant binary-level image after the MSLM with a stored image of Fig.8(c) was illuminated uniformly with light to bring quadrant 4 to the level of quadrant 2 and thresholding was again employed to restore quadrants 1 and 3 back to zero.

Figures 8(e) and (f) illustrate contrast reversal. In both cases, the images were written by electron accumulation. The crystal was first biased, by means of secondary electron emission, with a uniform positive-charge background at either a minimum in the transmittance characteristic [Fig.8(e)] or at maximum transmittance [Fig.8(f)].

Figures 8(g) and 8(h) illustrate contrast enhancement. In Fig.8(g) the image shown in Fig.8(e) was washed out with background illumination. Figure 8(h) shows the contrast-enhanced result after analog thresholding. Figures 8(i) and 8(j) illustrate edge enhancement of a binary-level image. Figure 8(i) results from Fig.8(e) when the write-image exposure corresponds to the full-wave surface-charge density  $\sigma_{2\pi}$ ; similarly, Fig.8(j) results from Fig.8(f) for the full-wave input-image exposure.

Figures 8(m)-8(r) illustrate the AND, NAND, OR, NOR, XOR, and NXOR operations of the horizontal and vertical bar images shown in Figs.8(k) and 8(l). Except for Figs.8(o) and 8(p), all the images were achieved in a device without an acceleration grid. Further details of how the above

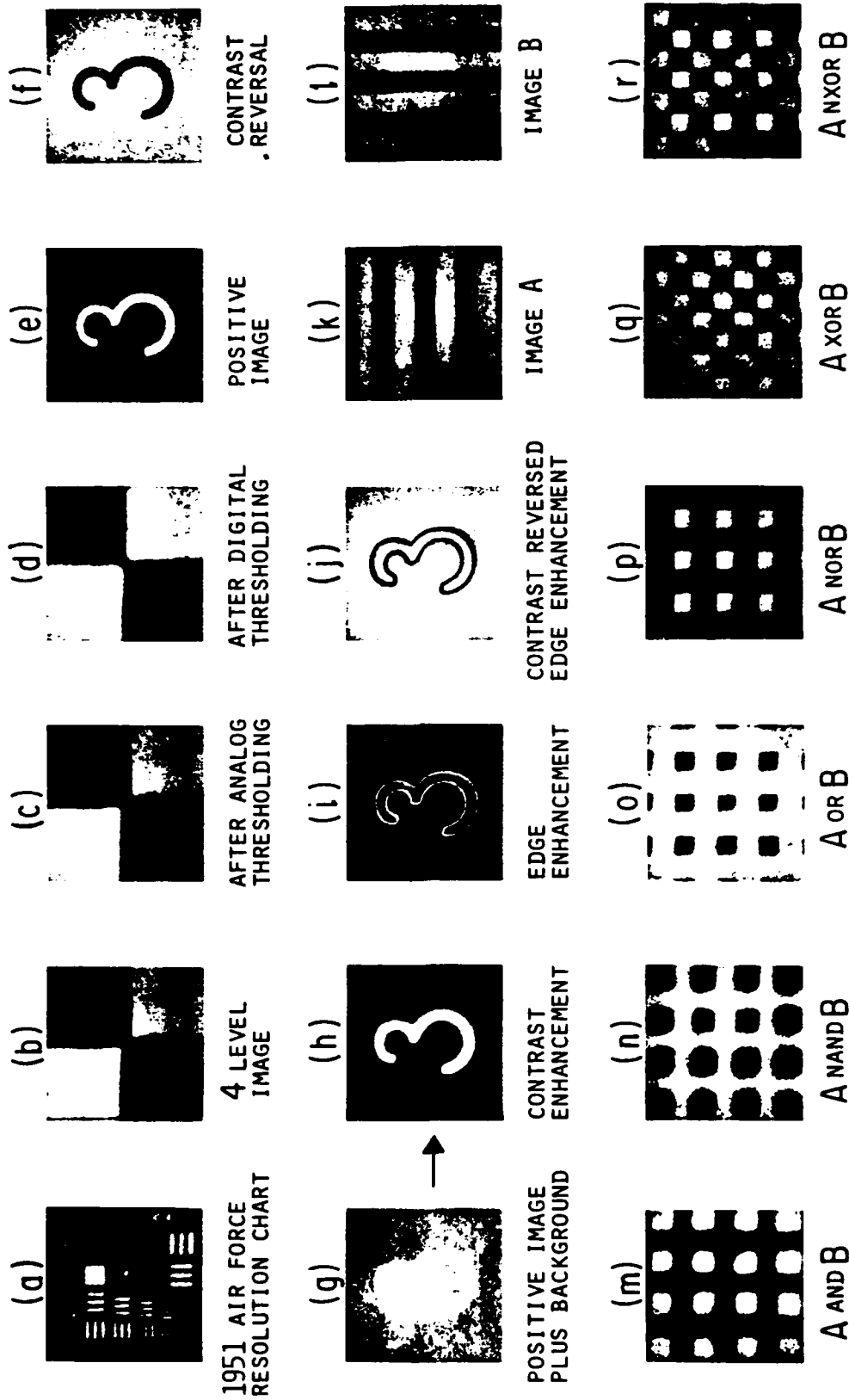


Fig 8. Some of the open-loop information processing operations that have been achieved by operating the MSLM in its space domain information processing mode.

operations were achieved are given in Ref. 2.

The image-processing operations presented in Fig.8 were obtained using a vacuum-demountable prototype device with a 330- $\mu\text{m}$ -thick oblique-cut  $\text{LiNbO}_3$  crystal. This device employed a single dielectric mirror on the crystal, and was read out between crossed polarizers. The MCP used had a strip current of 250 $\mu\text{A}$  and a gain of  $1.1 \times 10^4$  at 1kV of bias. The device was studied with and without an acceleration grid. The grid had a spatial frequency of 30 wires/mm.

The strip-current-limited framing rate of this device with the grid at 2 kV was 30Hz at full modulation depth and 60Hz at 50% modulation depth. The corresponding halfwave write (electron accumulation) and erase times were 10 and 23 msec, respectively. Its measured normalized light-to-light coherent MTF was found to have a value of approximately 1.9 cycles/mm at 50% contrast for a gap  $\ell_g$  of 500 $\mu\text{m}$ . Similar resolution results were obtained with the gridless device.

#### Limitations of the Space-domain Processing Mode

The fidelity of the space domain processing operations described above is strongly dependent on the energy distribution  $n(I_w, V_k, V_a, V_g)$  of the primary electrons, the secondary electron emission characteristics of the grid and the surface that receives the array of primary electron beams, the readout-intensity-vs.-surface-charge-density characteristic, and the spatial resolution of the device.

Sharp well-defined thresholds are achieved when the threshold voltage spread  $\Delta V_T$  is much smaller than the crystal halfwave voltage  $V_{\pi R}$ . Ideally, for a sharp, well-defined thresholding level, the array of primary electron beams incident on the mirror should be monoenergetic. Additionally, the secondary electron emission ratio for the grid should be small and that for the mirror surface should have a maximum value that is much greater than unity. Unfortunately, the majority of the output electrons from straight-channel microchannel plates have a considerable energy spread (0 to  $> 50\text{eV}$ ).<sup>4,5</sup> Thus, sharp thresholds are not expected from straight-channel MCPs. Better defined threshold levels are expected from curved channel MCPs which should have a much smaller output electron energy spread. In the current oblique-cut  $\text{LiNbO}_3$  MSLMs that employ straight-channel MCPs,  $\Delta V_T \approx 100\text{V}$  and  $V_{\pi} = 1250\text{V}$ .

The readout-intensity-vs-surface-charge-density characteristic can also be of considerable importance in space domain processing when the electron accumulation write mode is used. For example, the sharp OFF to ON characteristic of the Fabry-Perot crystal [see Fig. (6)] permits hard clipping to be accomplished in the electron accumulation write mode when the initial readout background or bias intensity is set at a null.

Severe degradation in image sharpness can result during space domain processing if care is not exercised to prevent stray secondary electrons from being attracted back to the mirror surface, or if the gap voltage  $V_g$  becomes so small that proximity focussing of the primary electrons is lost. It is, therefore, advantageous to have a priori knowledge of the intensity dynamic range of the write information when real-time space domain processing is being attempted.



## MATERIALS LIMITATIONS

The versatility of the MSLM is derived from the unique architecture of the device which permits one to choose materials for the photocathode, MCP, grid, dielectric mirror and the electro-optic crystal that are best suited for the application in question. We shall discuss each of these in turn.

### Photocathode

The input window and photocathode material determine the write light wavelength response of the MSLM. Typical photocathode/window combinations span the wavelength range between 110 and 1200 nm. Fortunately, MCPs respond directly to radiation in the mid ultraviolet and soft x-ray regions and therefore no photocathode is needed in these regions.<sup>7,3</sup> Beyond 1300nm no photocathode exists and consequently the MSLM cannot process infrared signals with wavelengths beyond this cutoff value.

### Microchannel Plate

A microchannel plate (MCP) is an imaging electron multiplier that preserves the relative spatial distribution of the input electron flux. It is essentially a thin (0.5 - 1.0 mm) wafer of semiconducting glass channels that is electroded on both faces. A typical MCP may have 10- $\mu$ m-diameter pores on 15  $\mu$ m center to center spacing packed in a hexagonal array. Both straight and curved channel<sup>9</sup> MCPs are manufactured. In straight channel plates, the pores are generally slanted at an angle of about 5-15° away from the plate normal. The typical length-to-diameter ratio of the pores is about 40 to 1. Plates as large as 15cm in diameter have been manufactured.

The strip current  $I_s$  is that current which flows through the plate when no electron or photon is incident on the plate. The typical strip current for a 25-mm-diameter straight channel plate is about 10 $\mu$ A at 1kVDC of bias. Under steady state dc operation, the unsaturated MCP output current density  $J_0$  is

given by

$$J_0 = I_w neG/h\nu$$

where  $I_w$  and  $\nu$  are the intensity and frequency of the write light respectively,  $h$  is Planck's constant,  $e$  is the electronic charge,  $\eta$  is the quantum efficiency of the photocathode and  $G$  is the gain of the MCP. In continuous mode operation the extracted current from the MCP is generally less than one-fifth of the strip current.

In pulsed-mode applications, pulsing the strip current can result in output current pulses as high as  $1 \text{ A/cm}^2$ .<sup>10</sup> For high gain applications, two straight channel plates may be cascaded in a proximity focus configuration. Recently, curved channel plates<sup>9</sup> operating at 2 kV of bias with strip currents of 30  $\mu\text{A}$  and gains of  $10^6$  have been replacing the cascaded configuration.

The framing speed of the MSLM is generally limited by the available output current of the MCP. And, since the MCP output current is derived from the strip current, high strip current is often more desirable than high gain. The MCP strip current depends on the resistivity of the channels, and special post-manufacturing reduction processes can be employed to lower the resistivity of the pores and thereby increase the strip current without a substantial reduction of the gain of the plate. Straight channel MCPs with strip currents up to 300  $\mu\text{A}$  have been employed in MSLMs. To avoid thermal runaway, care must be exercised when using plates with such high strip currents.

Since there has not been a great demand for high strip current MCP's, very few of them have been produced, and little, if any, systematic research has been done on the development of these items. Such an effort is clearly warranted at this time.

### Acceleration Grid

The ideal requirements of the acceleration grid are large fractional open area, high tensile strength, low elasticity, and low secondary electron emission yield. In general, a metal mesh (e.g. of copper or nickel) is chosen as the grid material.

High tensile strength is required because the electrostatic forces acting on the grid during operation can be quite large. More specifically, it can be shown that the electrostatic force per unit area  $\bar{F}$  acting on a planar grid which is held at a potential  $V_a$  and positioned at distances  $\ell_m$  and  $\ell_g$  from the MCP output electrode and the free surface of the crystal respectively, is given by<sup>11</sup>

$$\bar{F} = \frac{1}{2}\epsilon_0[(V_g/\ell_g)^2 - (V_a/\ell_m)^2] \quad (11)$$

$$= \frac{1}{2}\epsilon_0 \left[ \left[ \frac{\frac{\epsilon_{11}}{\ell_x}(V_b - V_a) + \sigma/\epsilon_0}{1 + \frac{\ell_g}{\ell_x}\epsilon_{11}} \right]^2 - \left[ \frac{V_a}{\ell_m} \right]^2 \right] \quad (12)$$

where  $\ell_x$  and  $\epsilon_{11}$  are the thickness and dielectric constants respectively of the crystal in the longitudinal direction, and  $\epsilon_0$  is the permittivity of free space. In Eq. 12,  $\bar{F}$  is positive when the force is in the direction of the crystal and it increases when electrons are removed from the mirror. For typical MSLM parameters ( $\ell_m = \ell_g = 0.5\text{mm}$ ,  $\ell_x = 0.1\text{mm}$ ,  $\sigma = \sigma_{\pi} = +0.42\mu\text{C}/\text{cm}^2$ ,  $\epsilon_{11} = 38$ ,  $V_b = 5\text{kV}$ , and  $V_a = 2\text{kV}$ ) we find  $\bar{F} = 0.025 \text{ Newton}/\text{cm}^2$ .

Low elasticity and high tensile strength are therefore important requirements so that the grid does not deform significantly, which would cause an increase in the force. Clearly, the need to maintain a small gap between the MCP and the

crystal to assure good proximity focussing, and at the same time the need to employ a large enough gap so that the grid does not touch or arc to either the surface of the MCP or the crystal during operation are the constraints that set the upper and lower limit on the dimensions of the gap.

### Dielectric Mirror

Dielectric mirrors consist of alternating layers of high and low refractive index dielectric materials. In the MSLM design shown in Fig.1, the electrons are deposited on the dielectric mirror. Ideally, then, the dielectric mirror should have high damage resistance under electron beam bombardment, negligible electron beam induced conductivity, large secondary electron yield, high reflectivity at the readout wavelength, low vapor pressure, and, to avoid cracking and flaking, low internal stresses when cycled up and down in temperature. Several combinations of materials exist that satisfy these requirements.

### Electro-Optic Crystal

The performance of the MSLM is determined more by the electro-optic crystal than by any of the other components. The crystal in the MSLM, like that in other electro-optic spatial light modulators, is operated in the longitudinal electro-optic mode. That is, the readout light and the applied electric field component of interest are parallel. The electro-optic crystal within the MSLM is addressed through the dielectric mirror by the charge distribution on the surface of the mirror, and therefore, the half-wave surface charge density is often a better figure of merit for comparing crystals than the halfwave voltage.

The halfwave longitudinal surface charge density  $\sigma_\pi$  is the charge density at the surface of the dielectric mirror that gives rise to a phase retardation of  $\pi$  radians in the electro-optic crystal. The halfwave surface charge density is related to the halfwave voltage  $V_\pi$  via the capacitance per unit area  $\bar{C}$  of the crystal by  $\sigma_\pi = \bar{C}V_\pi$ .

When amplitude and phase modulation are achieved by modulating the birefringence of the crystal and reading out the crystal between crossed polarizers, the phase retardation for amplitude modulation  $\Gamma_a$  is given by

$\Gamma_a = \Delta\phi_{x'} - \Delta\phi_{y'}$ , where  $\Delta\phi_{x'}$  and  $\Delta\phi_{y'}$  are the phase changes produced along the induced dielectric axes,  $x'$  and  $y'$ , of the crystal. Phase-only modulation with such a crystal is achieved by reading out the device with light polarized along either the  $x'$  or  $y'$  axis. Then the phase retardation for phase modulation  $\Gamma_p$  is given either by  $\Gamma_p = \Delta\phi_{x'}$  or by  $\Gamma_p = \Delta\phi_{y'}$ . In z-cut  $\overline{4}2m$  crystals, for example,  $\Delta\phi_{x'} = -\Delta\phi_{y'}$ , hence  $\Gamma_p = \frac{1}{2}\Gamma_a$ , and so  $\sigma_{\pi p} = 2\sigma_{\pi a}$ . Also, since the MSLM is a reflex mode device, the readout light makes a double-pass through the crystal and hence  $\sigma_{\pi R} = \frac{1}{2}\sigma_{\pi}$ , where  $\sigma_{\pi R}$  is the reflex half-wave surface charge density.

### Lithium Niobate

$\text{LiNbO}_3$ , a crystal of the 3m point group, has been the electro-optic material most frequently used to date in the MSLM. The symmetry of this crystal makes the z-cut material fairly well suited for phase modulation because the longitudinal component of the electric field modulates  $\Delta\phi_{x'}$  and  $\Delta\phi_{y'}$  symmetrically. That is, the index ellipsoid remains cylindrically symmetric when longitudinal fields are applied along the z-axis. Therefore, in principle, there is no need to polarize the readout light for phase modulation with this crystal cut. In practice, however, transverse fields, which are always present in non-uniform surface charge distributions, cause an additive phase modulation error. Fortunately, the dielectric mirror has a shielding effect, since the strongest transverse fields are confined within the dielectric mirror layer.

To achieve intensity modulation with the z-cut crystal, an interferometric or a Schlieren readout configuration may be used. An interferometric

readout scheme that works fairly well involves interference between the back and front surface reflections (15% reflectivity at normal incidence) from a plane parallel crystal.

For z-cut LiNbO<sub>3</sub> operated in the reflex mode with longitudinal fields, the phase retardation  $\Gamma_{pR}$  due to a longitudinal field  $E_z$  is given by

$$\Gamma_{pR} = \Delta\phi_x = \Delta\phi_y = \frac{2\pi}{\lambda} n_0^3 r_{13} E_z \ell_x \quad (13)$$

and hence

$$V_{\pi R} = \frac{\lambda}{2n_0^3 r_{13}} \quad \text{and} \quad \sigma_{\pi R} = \frac{\epsilon_0 \epsilon_{\parallel} \lambda}{2n_0^3 r_{13} \ell_x} \quad (14a); (14b)$$

where  $\epsilon_0$  is the permittivity of free space,  $\epsilon_{\parallel}$  is the dielectric constant of LiNbO<sub>3</sub> along the field direction,  $\lambda$  is the wavelength of the readout light, and  $n_0$ ,  $\ell_x$  and  $r_{13}$  are respectively the ordinary refractive index, thickness and electro-optic coefficient of the LiNbO<sub>3</sub> wafer. For z-cut LiNbO<sub>3</sub>,  $r_{13} = 8.6 \times 10^{-12} \text{ m/V}$ ,  $n_0 = 2.28$  at 633nm wavelength, and  $\epsilon_{\parallel} = 30$ . Thus  $V_{\pi R} = 3100$  volts, and for a 100 $\mu\text{m}$ -thick crystal,  $\sigma_{\pi R} = 0.8 \mu\text{C/cm}^2$ .

The halfwave voltage and the halfwave surface charge density for intensity modulation can be reduced significantly by employing the crystal cut which optimizes the phase retardation. It can be shown that the optimum cut is such that the normal to the plate lies in the x-y plane, and is rotated about the x-axis by 55° from the +z towards the -y axis.<sup>12</sup> For this cut, the calculated value of  $V_{\pi R}$  is 1150 volts which compares favorably with our measured values of 1250 volts.<sup>3</sup> It should be pointed out that for this cut  $|\Delta\phi_x| \neq |\Delta\phi_y|$ , and therefore, even with longitudinal fields only, this crystal cut will not lead to an amplitude-only modulator. That is, there would always be a signal-dependent phase error accompanying the amplitude modulation.

Ideally, for MSLM applications the electro-optic crystal should have small dielectric constants, large electro-optic coefficients which couple only to longitudinal electric fields, high surface and bulk resistivity, high dielectric strength, good optical quality, good mechanical strength and hardness, small temperature coefficients, insolubility in the common solvents, low vapor pressure and good bakeability up to about 400°C.

Unfortunately, because of the coupling between the dielectric constants and the electro-optic coefficients in most materials, any steps taken to increase the electro-optic coefficients (e.g. by operating near the Curie temperature) always result in a concomitant increase in the dielectric constant, and, in general, design tradeoffs must be made. Additionally, both the spatial resolution and the capacitance increase with decreasing crystal thickness, and because the primary current is limited by the MCP strip current, tradeoffs between speed and resolution are often necessary. Research on new electro-optic materials for spatial light modulation and on new ways of employing existing materials is sorely needed at this time.



# Electro-optic Materials Comparison

Almost any electro-optic material can be employed in the MSLM, and the choice of material would be dictated by the intended application. Nevertheless, in Table I we list and compare some of the properties of importance to the MSLM for the common electro-optic crystals used in spatial light modulators today. The materials chosen for comparison are z-cut deuterated potassium dihydrogen phosphate (DKDP), which is used in the photo DKDP light valve,<sup>13</sup> <001>-cut Bismuth silicon oxide (BSO), which is used in PROM,<sup>14</sup> and z-cut and 55°-cut lithium niobate, which have been used in the MSLM.<sup>2,3</sup> DKDP is generally used near its Curie temperature (-51°C) in spatial light modulator applications.

Table I. Materials Comparison

MATERIAL PROPERTY	Z-CUT DKDP ( $\bar{4} 2 m$ ) (25°C) (-51°C)		<001>-CUT BSO (2 3) (25°C)	Z-CUT LiNbO <sub>3</sub> (3 m) (25°C)	55°C CUT LiNbO <sub>3</sub> (3 m) (25°C)
$\epsilon_{  }$ $\epsilon_{\perp}$	50 58	650 65	56 56	29 44	36 44(max)
$(\epsilon_{  }/\epsilon_{\perp})^{1/2}$	0.9	3.2	1.0	0.8	0.9
$\rho_{  }$ $\rho_{\perp}$ ( $\Omega$ cm)	$10^{11}$ --	$5 \times 10^{13}$ $1 \times 10^{13}$	$5 \times 10^{13}$ (dark)	$>10^{15}$	$>10^{15}$
BREAKDOWN FIELD (kV/cm)	5-10		--	~500	~500
REFLEX HALFWAVE VOLTAGE $V_{\pi R}$ ( $\lambda = 0.633\mu m$ )	$\Delta\phi_x - \Delta\phi_y = \pi$ $\frac{\lambda}{4n_o^3 r_{63}}$ 1700 125		$\Delta\phi_x - \Delta\phi_y = \pi$ $\frac{\lambda}{4n_o^3 r_{63}}$ 1950	$\Delta\phi_x = \Delta\phi_y = \pi$ $\frac{\lambda}{2n_o^3 r_{13}}$ 3100	$\Delta\phi_x - \Delta\phi_y = \pi$ $\frac{\lambda}{2(f_x - f_y)}$ 1250
$\sigma_{\pi R}$ ( $\mu C/cm^2$ ) ( $\ell_x = 100\mu m$ )	0.8	0.8	1.0	0.8	0.42
$Q_{\pi}$ (nC/pixel) ( $\ell_x = 100\mu m$ )	0.97	0.08	0.99	1.2	0.51

In the table,  $\epsilon_{\parallel}$  and  $\epsilon_{\perp}$ , and  $\rho_{\parallel}$  and  $\rho_{\perp}$  are the dielectric constants and resistivities parallel and perpendicular respectively to the longitudinal electric field. To a good approximation, it can be shown that for electro-optic materials with large dielectric constants the MSLM spatial resolution MTF rollover point  $N_1$  (cycles/mm) is given by

$$N_1 \approx \frac{1}{\pi \ell_x} (\epsilon_{\parallel}/\epsilon_{\perp})^{\frac{1}{2}} \quad (15)$$

Here, the quantity  $(\epsilon_{\parallel}/\epsilon_{\perp})^{\frac{1}{2}}$  is used as a crystal resolution parameter in Table I. Note that by cooling DKDP near its Curie temperature, its resolution parameter increases significantly.

The halfwave voltage and the halfwave surface charge density are also given in Table I. Note that because z-cut  $\text{LiNbO}_3$  remains uniaxial when a longitudinal field is applied, we have chosen to calculate its halfwave voltage and charge density that correspond to an absolute change in phase of  $\pi$  radians for either x or y polarized light. Note also that 55°-cut  $\text{LiNbO}_3$  offers the lowest halfwave surface charge density and hence the reason for our interest in this crystal cut. On the other hand, the switching charge per pixel which is also provided in Table I, is given by  $\bar{Q}_{\pi} = \sigma_{\pi R}/N_1^2$ , and is smallest for cooled DKDP. The write light switching energy per pixel  $\bar{E}_{\pi}$  is given by

$$\bar{E}_{\pi} = \frac{\bar{Q}_{\pi} h\nu}{\eta eG} \quad (16)$$

where we have assumed  $J_p = J_0$ . For the 55°-cut  $\text{LiNbO}_3$  example shown in Table I, taking  $\lambda = 633\text{nm}$ ,  $\eta = 0.1$  and  $G = 10^4$ , we find that the calculated value of  $\bar{E}_{\pi}$  is 1.0pJ/pixel.

## APPLICATIONS TO ADAPTIVE PHASE COMPENSATION

Atmospheric optical communications theory<sup>15-19</sup> and propagation studies<sup>20-23</sup> suggest that adaptive phase compensation may considerably improve the performance of optical communications links through such low-visibility conditions as snow, rain, fog or smoke. An adaptive phase compensated receiver essentially senses the spatial phase distortions in the scattered light arriving at the receiver, and uses a spatial phase modulator to "straighten out" the distortions in the wavefront. The compensated wave can then be processed by a diffraction-limited field of view (FOV) receiver (e.g. heterodyne) with very little collection of the background light which arrives from a wide FOV. Therefore, such a scheme results in an improvement of the communication signal-to-noise-ratio.

A million or more compensated elements are generally required to correct a low-visibility receiver aperture of only a few centimeters diameter.<sup>19-23</sup> The conventional adaptive optical technology<sup>24</sup> consisting of an array of discrete phase modulators cannot practically be extended to these high resolutions. Therefore, an "all-optical" parallel processing approach, which employs a sensitive optically-addressed spatial light modulator (Microchannel Spatial Light Modulator) and a new phase measurement and compensation technique (Interference Phase Loop), was investigated.

### All Optical System

Figure 9 is a conceptual diagram of an "all optical", phase-compensated direct-detection communications receiver. The received wavefront of the scattered light passes through an optically-addressed monolithic spatial light modulator which adds the appropriate phase to present a compensated, approximately planar wavefront to the direct-detection receiver. Part of

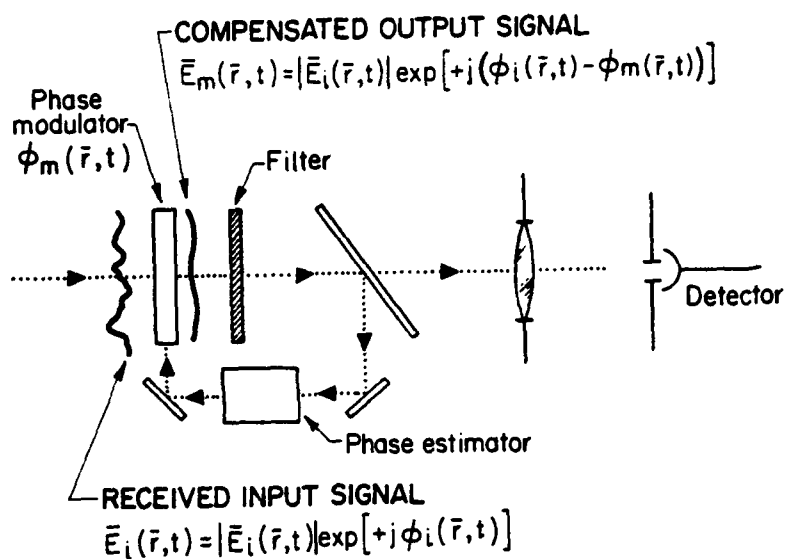


Fig 9. Direct-detection phase compensated receiver.

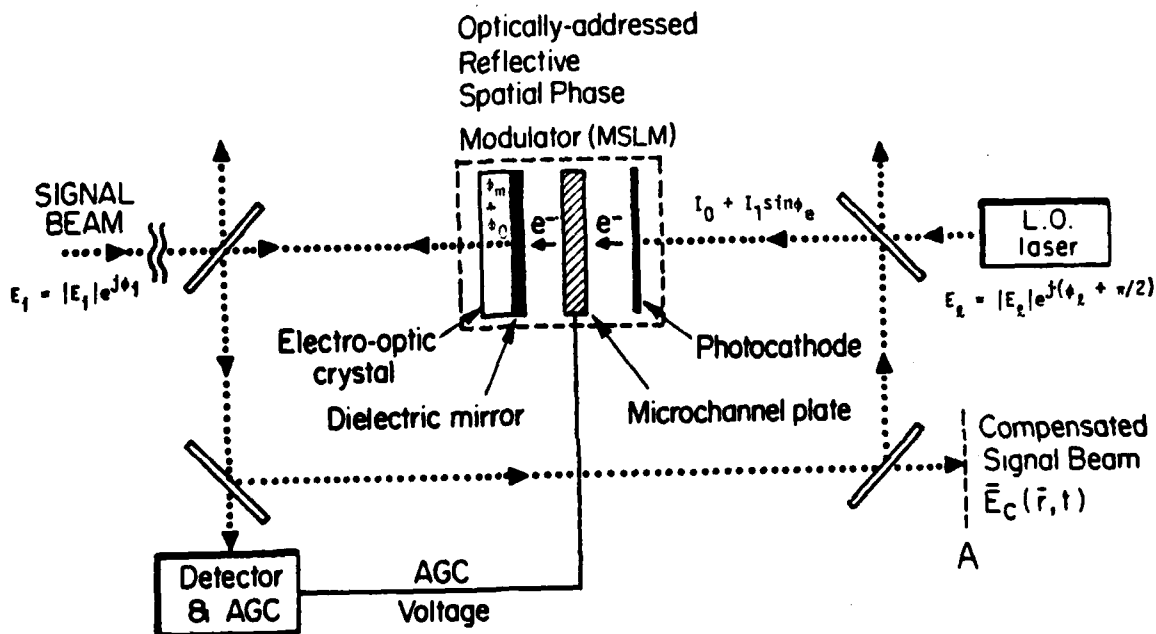


Fig 10. An all-optical high resolution interference phase loop employing an MSLM.

the compensated wavefront is fed back into the box labeled "phase estimator" whose output is an optical signal proportional to the phase of the compensated beam. This optical control signal drives the spatial light modulator.

Most existing phase measurement techniques<sup>6</sup> either have undesirable performance limitations or are too complicated to be implemented in the phase estimator of Fig. 9. For example, elementary phase visualization techniques such as Zernike phase-contrast, heterodyne, homodyne, shearing, and polarization interferometry are all-optical; however, they cannot by themselves distinguish wavefront phase from amplitude variations. They also suffer from a nonlinear dynamic range of  $\pi$  radians as well as from  $2n\pi$  and phase quadrant ambiguities.

Recently, we have recognized (see Refs. 25 and 26 which are reproduced in Appendices III and IV) that there exists a class of closed loop configurations similar to Fig. 9 that possesses inherent properties which simplify phase estimation and compensation. In these closed loop configurations, called Interference Phase Loops (IPL), phase estimation and phase compensation are achieved simultaneously by using the output of an elementary interferometer to drive a phase-only modulator in the path of the wavefront to be measured or compensated. Figure 9 therefore becomes an example of an IPL when the "phase estimator" is an elementary two-beam interferometer.

Theoretical and experimental studies have shown<sup>6,25,26</sup> that the IPL not only largely ignores amplitude fluctuations, but also has no phase quadrant ambiguity and can continuously estimate phase over multiple  $\pi$  radians of dynamic range. When self-interference is employed (e.g. Zernike phase contrast), monochromatic light is not required. In operation, the drive signal to the IPL phase modulator and the output intensity from the elementary interferometer become representations of the phase estimate. In many respects,

the IPL can be considered as an optical phase-locked loop which directly tracks optical wavefront phase.

Figure 10 illustrates a specific all-optical implementation of the IPL employing a homodyne interferometer and a reflection readout spatial phase modulator, the MSLM. Figure 11 is a low-resolution demonstration of all-optical phase compensation with an MSLM/IPL system. The prototype MSLM that was used employed an electrooptic crystal ( $\text{LiTaO}_3$ ) with parallel faces and without a dielectric mirror. The reflection from the front crystal face provided a homodyne L.O. beam, which allowed the nonuniform internal phase distortion,  $\phi_0(x,y)$ , of the crystal to be compensated. (This parallel-face structure is actually a low finesse Fabry-Perot interferometer.<sup>6</sup>) Figure 11a is an interferogram of the initially uncompensated phase distribution, which had a dynamic range of about  $\pi$  radians. The compensated interferogram in Fig. 11b was recorded with the same exposure as Fig. 11a, and the longer exposure (12 times larger) of Fig. 11c reveals that the residual phase error is very small ( $\sim \lambda/10$  or  $\lambda/20$ ).

Unfortunately, general real-time high-resolution compensation could not be demonstrated with this prototype MSLM, because the parallel-crystal Fabry-Perot reflections produce undesirable<sup>11</sup> intensity modulation in an external interferometer. Now that high quality prototype MSLMs with oblique cut  $\text{LiNbO}_3$  crystals are available, truly high resolution all-optical phase compensation should be achievable in the near future.

## PHASE COMPENSATED RESULTS WITH ALL-OPTICAL IPL/MSLM SYSTEM

UNCOMPENSATED



(A)

EXPOSURE: 1/8 SEC

COMPENSATED



(B)

1/8 SEC

COMPENSATED



(C)

1.5 SEC

- (A) OPEN LOOP INTERFEROGRAM OF PHASE DISTORTION  $\psi_0(\vec{r})$  OF ELECTRO-OPTIC CRYSTAL IN AN EARLY MSLM.
- (B) CLOSED LOOP (IPL) INTERFEROGRAM ILLUSTRATING PHASE COMPENSATION OF THE DISTORTION SHOWN IN (A).
- (C) LONG-TERM EXPOSURE OF (B) TO SHOW RESIDUAL ERROR.

NOTE: FRINGES IN LOWER LEFT OF (A) AND (C) DUE TO INTERFERENCE BETWEEN MCP AND CRYSTAL SURFACES AND ARE NOT WITHIN THE OPTICAL FEEDBACK PATH.

(NO DIELECTRIC MIRROR USED IN THIS DEVICE.)

Fig 11. Phase compensation results with the all optical IPL/MSLM system.

## REFERENCES

1. J. L. Wisa, Nucl. Instrum. Methods 162, 587 (1979).
2. C. Warde, A. M. Weiss, A. D. Fisher, and J. I. Thackara, Appl. Opt. 20, 2066 (1981).
3. C. Warde and J. I. Thackara, Opt. Lett. 7, 344 (1982).
4. A. J. Guest, Acta Electron. 14, 79 (1971).
5. A. M. Tyutikov and L. B. Tsoi, Sov. J. Opt. Technol. 43, 86 (1976).
6. A. D. Fisher, "Techniques and Devices for High-Resolution Adaptive Optics," Ph.D. Thesis, Massachusetts Institute of Technology, August 1981.
7. P. J. Bjorkholm, L. P. VanSpeybroeck and M. Hecht, Proc. SPIE 108, 189 (1977).
8. K. W. Dolan and J. Chang, Proc. SPIE 106, 178 (1977).
9. J. G. Timothy, Rev. Sci. Instrum. 52, 1131 (1981).
10. B. Leskovar, Phys. Today 30, 42, No.11, Nov (1977).
11. J. I. Thackara, "Image Processing Characteristics of the Microchannel Spatial Light Modulator," M.S. Thesis, Massachusetts Institute of Technology, June 1982.
12. K. F. Hulme, P. H. Davies and V. M. Cound, J. Phys. C2, 855 (1969).
13. D. Casasent, Opt. Eng. 17, 365 (1978).
14. B. A. Horwitz and F. J. Corbett, Opt. Eng. 17, 353 (1978).
15. R. S. Kennedy, "Communication through Optical Scattering Channels: an introduction, " Proc. IEEE, 58, 10, 1651-1665, 1970.
16. S. R. Robinson, "Spatial Phase Compensation Receivers for Optical Communication," Ph.D. Thesis, M.I.T., E.E. Dept., May 1975.
17. S. R. Robinson, "Phase Compensation Receivers for Optical Communication," IEEE Trans. on Communications, COM -25, 900-909, 1977.



18. C. Warde and A. D. Fisher, "Adaptive Phase Compensation for Low-visibility Optical Communication," Proc. of the SPIE, 209, 144-151, 1979.
19. J. H. Shapiro and C. Warde, "Optical Communication through Low-visibility Weather," Opt. Eng., 20, 1, 1981.
20. W. H. Paik, M. Tebyani, D. J. Epstein, R. S. Kennedy and J. H. Shapiro, "Propagation Experiments in Low Visibility Atmospheres," Appl. Opt., 17, 899-905, 1978.
21. C. G. Mooradian, M. Geller, L. B. Stotts, D. H. Stevens, and R. A. Krautwald, "Blue-Green Pulsed Propagation Through Fog," Appl. Opt., 18, 429-441, 1979.
22. J. Nakai, "A Spatio-Temporal Channel Model of Low-visibility Optical Wave Propagation," S.M. Thesis, Dept. of Electrical Engineering and Computer Science, M.I.T., January 1980.
23. W. S. Roxx, W. P. Jaeger, J. Nakai, T. T. Nguyen and J. H. Shapiro, "Atmospheric Optical Propagation: An Integrated Approach," Submitted to Opt. Eng.
24. J. W. Hardy, "Active Optics: A New Technology for the Control of Light," Proc. IEEE, 66, 651-697, 1978.
25. A. D. Fisher and C. Warde, "Simple Closed-loop System for Real-time Optical Phase Measurement," Optics Lett., 4, 131-133, 1979.
26. A. D. Fisher and C. Warde, "Technique for High-Resolution Adaptive Phase Compensation," Optics Letters, 8, 353-355, 1983.

COLLABORATION WITH RELATED RESEARCH GROUPS

In the past one and one-half years, we continued our fruitful discussions with Professor Armand Tanguay of the University of Southern California on (1) MSLM design modifications, (2) the spatial resolution of electro-optic spatial light modulators, and (3) phase and amplitude modulation errors in electro-optic spatial light modulators due to the transverse components of the electric field in the crystal.

We have also continued the discussions with personnel at Lockheed Corporation on the application of the MSLM to atmospheric phase compensated optical communication through the atmosphere and with General Dynamics, Pomona division, on the spatial filtering applications of the MSLM.

PUBLICATIONS RESULTING FROM AFOSR SPONSORSHIP

1. C. Warde, A. D. Fisher, D. M. Cocco and M.Y. Burmawi, "Microchannel Spatial Light Modulator," Optics Letters, 3, No. 5, 196 (1978).
2. C. Warde, A. D. Fisher, D. M. Cocco and M. Y. Burmawi, "Development of the Microchannel Spatial Light Modulator," Proceedings of the International Optical Computing Conference, London, September 1978, pp. 13-34.
3. C. Warde and A. D. Fisher, "Microchannel Spatial Light Modulator as a Storage Medium," Proc. SPIE, Vol. 177, pp. 67-69, (1979).
4. \*C. Warde, and A. D. Fisher, "Adaptive Phase Compensation for Low-visibility Optical Communication," Proc. SPIE, 209, 144-151, 1979.
5. C. Warde, "An MSLM for Optical Information Processing," Optical Spectra, February 1980, pp. 63-69.
6. C. Warde, A. M. Weiss and A. D. Fisher, " $\text{LiNbO}_3$  and  $\text{LiTaO}_3$  Microchannel Spatial Light Modulators," Proc. SPIE, 218, 59-66, 1980.
7. C. Warde and A. Fisher, "High-Resolution Adaptive Phase Compensation for Low-visibility Optical Communication," 1980 Electronics and Aerospace Systems Conference, (IEEE, New York), pp 539-545, 1980.
8. C. Warde, A. D. Fisher, J. I. Thackara and A. M. Weiss, "Image Processing Operations Achievable with the Microchannel Spatial Light Modulator," Proc. SPIE, 252, 25-32, 1980.
9. C. Warde, "Performance Limitations of the Microchannel Spatial Light Modulator," Proceedings of the 1980 European Conference on Optical Systems and Applications, Utrecht, The Netherlands, September 1980, in Proc SPIE, 236, 389-397, 1980.
10. C. Warde, A. M. Weiss, A. D. Fisher and J. I. Thackara, "Optical Information Processing Characteristics of the Microchannel Spatial Light Modulator," Applied Optics, 20, 2066-2074, 1981.

PUBLICATIONS RESULTING FROM AFOSR SPONSORSHIP

11. J. H. Shapiro and C. Warde, "Optical Communication through Low-visibility Weather," Optical Engineering 20, 76-83, 1981.
12. A. D. Fisher and C. Warde, "Techniques and Devices for Adaptive Phase Compensated Optical Communications," Proceedings of the NSF User-Grantee Meeting on Optical Communications, St. Louis, MO, May 1981, pp 29-37.
13. C. Warde, J. I. Thackara, "Oblique-cut LiNbO<sub>3</sub> Microchannel Spatial Light Modulator," Optics Letters, 7, 344-346, 1982.
14. A. D. Fisher and C. Warde, "Technique for High-Resolution Adaptive Phase Compensation," Optics Letters, 8, 353-355, 1983.

M.S. Theses

- D. M. Cocco, "Speed and the Resolution of a Microchannel-Addressed Optical Modulator," Aug. 1977.
- A. M. Weiss, "The Design and Construction of a Microchannel Spatial Light Modulator," Dec. 1980.
- J. I. Thackara, "Image Processing Characteristics of the Microchannel Spatial Light Modulator," June 1982.

Ph.D. Theses

- A. D. Fisher, "Techniques and Devices for High-Resolution Adaptive Optics," Aug. 1981.

LIST OF PERSONNEL

Faculty and Staff

Professor Cardinal Warde

Graduate Students

Stanley Rotman

Andrew Schwartz

John Thackara

Chon Meng Wong

Undergraduate Students

Robert Dillon

Thomas Grycewicz

Thomas Duffey

Chieh Lieh Lin

Shirley Young

Karl Chao

## APPENDIX I

# Optical information processing characteristics of the microchannel spatial light modulator

C. Warde, A. M. Weiss, A. D. Fisher, and J. I. Thackara

The microchannel spatial light modulator (MSLM) is a versatile, highly sensitive, and optically addressed modulator that is well suited for low-light level real-time optical information processing. The image processing operations that can be achieved with the MSLM include contrast reversal, contrast enhancement, edge enhancement, image addition and subtraction, analog and digital intensity level thresholding, and binary level logic operations such as AND, OR, EXCLUSIVE OR, and NOR. Several of these operations are demonstrated herein. Recent prototype MSLMs have exhibited a halfwave exposure of 2.2 nJ/cm<sup>2</sup>, an optical information storage time of more than two months, and a framing rate of 40 Hz with full modulation depth (200 Hz with 20% modulation depth). The role of secondary electron emission in the operation of the MSLM is discussed, and design modifications that would yield a spatial resolution of ~10 cycles/mm at the 50% point on an MTF curve are proposed.

## I. Introduction

The full exploitation of the inherent speed and parallel processing capability of optical systems has been impeded by the lack of satisfactory real-time reusable devices that can be used as substitutes for photographic film. Such devices are called spatial light modulators.

The microchannel spatial light modulator (MSLM) is a relatively new, versatile, highly sensitive, and optically addressed device that is well suited for low-light level real-time optical information processing. In addition to real-time operation, it can be designed to exhibit long term (months) optical information storage simultaneously. A variety of sophisticated image processing operations can be achieved with this device. These include contrast reversal, contrast enhancement, edge enhancement, image addition and subtraction, analog and digital intensity level thresholding, as well as binary-level logic operations such as AND, OR, EXCLUSIVE OR, and NOR.

The MSLM belongs to a class of spatial light modulators that converts an optical image into a charge dis-

tribution at a crystal-insulating layer interface. The charge distribution generates a voltage drop across the crystal at the expense of the voltage dropped across the insulating layer. The resulting electric field in the crystal modulates the refractive index of the crystal. The MSLM is unique in that it employs a microchannel plate to amplify the charge distribution before depositing it on the crystal; therefore, the insulating layer in the MSLM is constrained to be a vacuum gap.

It is the intent of this paper to describe the role of secondary electron emission in the operation of the MSLM, to give an update of its characteristics, and to describe and illustrate some of the important image processing operations that can be achieved with this device. Earlier stages of development of the MSLM have been reported.<sup>1-3</sup> Other real-time optically addressed spatial light modulators are reviewed elsewhere.<sup>4-6</sup>

## II. Device Description

The MSLM illustrated in Fig. 1 consists of a photocathode and a microchannel array plate (MCP) in proximity focus with a planar acceleration grid and an electrooptic plate. The electrooptic plate generally carries a high-resistivity dielectric mirror on one side and a transparent conducting electrode on the other. The MCP is an array of small (~10-μm) semiconducting-glass pores, each functioning as a continuous dynode electron multiplier.<sup>7,8</sup> Spatially uniform gains (±5% variation) of 10<sup>4</sup> with a single MCP or 10<sup>7</sup> with two cascaded MCPs (chevron configuration) are typical.<sup>9</sup>

In operation, the write light (coherent or incoherent) incident on the photocathode creates an electron image

The authors are with the Massachusetts Institute of Technology, Department of Electrical Engineering & Computer Science, Cambridge, Massachusetts 02139.

Received 30 October 1980.

0003-6935/81/122066-09\$00.50/0.

© 1981 Optical Society of America.

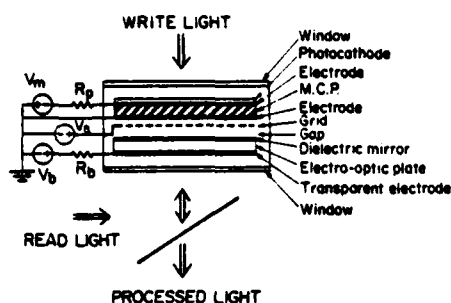


Fig. 1. Microchannel spatial light modulator.

which is amplified by the MCP and proximity focused onto the surface of the electrooptic plate. The resulting surface charge distribution creates a spatially varying electric field that modulates the refractive index of the electrooptic plate (crystal). Thus the readout light, which makes a double pass through the crystal, is spatially phase modulated.

The surface charge distribution may be either negative or positive depending on the operating conditions. Thus, two write modes are possible. In the electron-deposition write mode, the image is written by adding the appropriate electron distribution to the surface of the crystal; the image may be erased by secondary electron emission. In the inverted or secondary emission write mode, the image is written by employing secondary electron emission to remove the appropriate electron distribution from a uniformly charged crystal. In this case, erasure can be accomplished by simply adding electrons to the crystal.

Optical information that has been written into the MSLM may be read out either interferometrically with schlieren optics or with crossed polarizers. The possible readout modes depend on the symmetry and cut of the electrooptic crystal. The readout mode that is used in the prototype devices employs the interference between the front and back surface reflections from a plane-parallel electrooptic crystal. If dielectric mirrors are deposited on both sides of such a plane-parallel crystal to form a Fabry-Perot interferometer of finesse  $F$ , a complete off-to-on transition can be achieved with approximately  $1/F$  times the halfwave surface charge density of the crystal.

The MSLM can be either framed through a discrete sequence of write, read, and erase periods or operated in a continuous mode. In the framed mode, the optical write signal is integrated and stored in the form of a charge distribution. In the continuous mode of operation, which can be achieved with low resistivity crystals, the instantaneous modulation is proportional to the write image intensity for all temporal variations within the bandwidth of the system.

It is the wide choice of photocathodes and electrooptic materials that gives rise to the spectral versatility of the MSLM and permits its characteristics to be tailored for specific applications. For example, the wavelength of the write signal is limited only by the

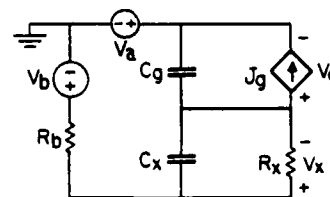


Fig. 2. Electrical-circuit model of an MSLM.

spectral response of existing photocathodes. No photocathode is needed in the extreme ultraviolet and x-ray regions since the MCP responds directly to this radiation.<sup>10,11</sup> The readout light is limited by the spectral transmittance of electrooptic materials (the range between the middle ultraviolet and the middle infrared).

Because of its large electron gain and its ability to integrate charge, the MSLM is capable of achieving the high photon sensitivities of image intensifier tubes. Devices employing one MCP are expected to be able to record visible images with intensities as low as  $10^{-14}$  W/cm<sup>2</sup>, the primary limitation being MCP dark current.

### III. Theory of Operation

An electrical-circuit model of an MSLM is shown in Fig. 2. The electrooptic crystals (LiTaO<sub>3</sub> and LiNbO<sub>3</sub>) that have been employed in the prototype devices have such high resistivity that  $R_x$  may be omitted. In this case all changes in  $V_b$  are divided capacitively between the crystal and the gap. That is,

$$V_b = V_g + V_x + V_a, \quad (1)$$

$$\Delta V_g = \frac{C_x}{C_g + C_x} \Delta V_b, \quad (2a)$$

$$\Delta V_x = \frac{C_g}{C_g + C_x} \Delta V_b. \quad (2b)$$

In general, the capacitance of the crystal is much higher than that of the gap, so a greater fraction of the change in  $V_b$  is coupled across the gap than across the crystal. The dependent current source of density  $J_g$  in Fig. 2 is the net current density in the gap. It is the sum of the primary current density  $J_p$  and the secondary emission current density  $J_s$ . The write and erase characteristics of the MSLM are determined, therefore, by the transport, electrooptical, and secondary emission properties of the crystal.

#### A. Monoenergetic System

The classical case of secondary emission from a floating target, at potential  $V_g$ , that is addressed with a monoenergetic electron beam from a cathode at potential  $-V_k$  ( $V_k > 0$ ) is discussed at length by Kazan and Knoll.<sup>12</sup> The energy of the primary electrons arriving at the surface of the target of such a system [see Fig. 3(a)] is  $E_p = e(V_k + V_g)$ , where  $e$  is the magnitude of the electronic charge.

\* After the modulation is read out the charge distribution

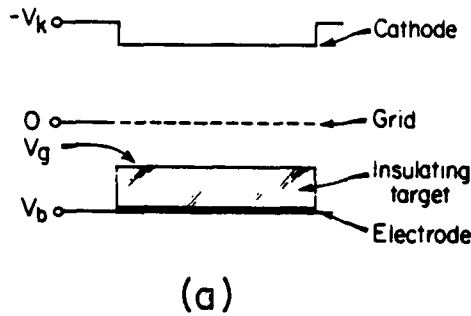
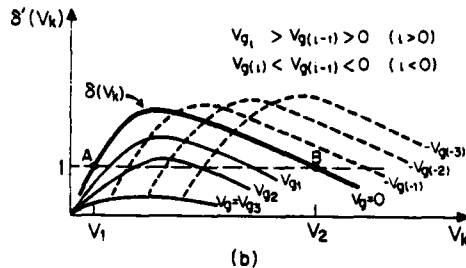


Fig. 3(a). Idealized, monoenergetic, electron-beam addressed insulating target system in which the secondary electrons are collected by a grid at ground potential.



3(b). Sketch of the ratio of collected secondary to primary electrons,  $\delta'(V_k)$ , for the floating surface of an insulating target system. Positive values of  $V_g$  are represented by the solid lines and negative values by the broken lines.

A sketch of the ratio of collected secondary to primary electrons,  $\delta'(V_k)$ , with  $V_g$  as a parameter, is shown in Fig. 3(b). The curve corresponding to  $V_g = 0$  is the conventional secondary electron emission coefficient  $\delta(V_k)$ , and its first and second crossover voltages are labelled  $V_1$  and  $V_2$ . The corresponding primary crossover energies are  $E_1 = eV_1$  and  $E_2 = eV_2$ . For insulators, the first crossover energy  $E_1$  typically falls in the 10–100-eV range and the peak value of  $\delta(V_k)$  generally varies between 1.5 and 25.<sup>12</sup>

The monoenergetic state-space plot shown in Fig. 4 has been adapted from Ref. 12. It shows how the initial kinetic energy  $eV_k$  of the primary electrons and the potential  $V_g$  of the floating surface must be adjusted to add or remove electrons from the target. External control of  $V_g$  can be achieved through  $V_b$  in accordance with Eq. (2a). In Fig. 4,  $E_1$  and  $E_2$  are the families of first and second crossover energies respectively of  $\delta'(V_k)$  for  $V_g \leq 0$ . Generally,  $E_1$  is relatively independent of  $V_g$  (i.e.,  $E_1' = E_1$ ), but  $E_2$  varies with  $V_g$ .<sup>12</sup>

When the monoenergetic system is operated in the regions where  $\delta' > 1$ , the target loses electrons and  $V_g$  decreases, whereas when  $\delta' < 1$  the target gains electrons and  $V_g$  increases. When  $\delta' = 1$ , the surface of the target stabilizes at some equilibrium voltage  $V_{eq}$ . The plot of Fig. 4 shows that there is one line of stable equilibria and one line of unstable equilibria that separate the regions  $\delta' < 1$  and  $\delta' > 1$ .

There are three distinct operating regions for the

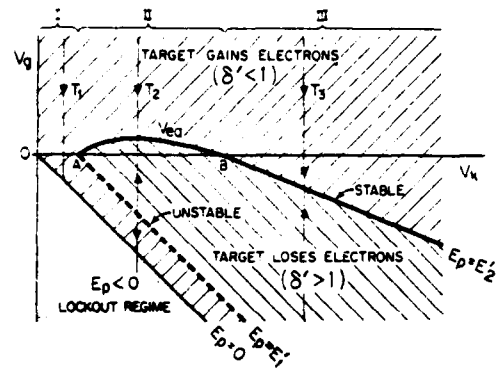


Fig. 4. State-space plot illustrating the behavior of a monoenergetic, electron-beam addressed, insulating target system.

monoenergetic system. These are separated by vertical boundaries (not shown) passing through the conventional crossover points A and B in Fig. 4:

(1) If  $eV_k < E_1$ , there is no adjustment of  $V_g$  that will result in the net removal of electrons from the target. This is because at high  $V_g$  most of the secondary electrons are attracted back to the target (that is,  $\delta' < 1$ ), and for low values of  $V_g$ , the low yield of secondary electrons directly results in  $\delta' < 1$ . Thus, if initially  $V_g > -V_k$ , electrons will accumulate on the target, and  $V_g$  will fall until the primary energy  $E_p$  becomes zero (that is,  $V_g \rightarrow -V_k$  or the potential drop across the target,  $V_x \rightarrow V_b + V_k$ ). This is illustrated by the trajectory  $T_1$  in Fig. 4. In the case where the system is operated with  $V_g < -V_k$ , no primary electrons can reach the target. This condition is called lockout.

(2) If  $E_1 < eV_k < E_2$  and the system is operated with large initial values of  $V_g$ , most of the secondary electrons will be attracted back to the target.  $V_g$  will fall, and  $\delta'$  will change until it eventually becomes unity at which point  $V_g$  stabilizes at its equilibrium value  $V_{eq}$ . Generally  $V_{eq}$  is only a few volts. If, on the other hand, the system is operated such that initially  $(E_1 - eV_k) < eV_g < eV_{eq}$ , then since  $\delta' > 1$  in this region, electrons will be removed from the target, and  $V_g$  will rise toward  $V_{eq}$ . Finally, if the system is operated such that  $-eV_k < eV_g < (E_1 - eV_k)$ , then since  $\delta' < 1$  in this region, the target will gain electrons, and  $V_g$  will fall until the primary electron energy becomes zero. The various regimes of  $V_g$  for this operating region are illustrated by the trajectory  $T_2$  in Fig. 4.

(3) In the case where  $eV_k > E_2$ , the behavior is similar to case 2 except that the equilibrium gap voltage is negative, and its magnitude can be very large, depending on the value  $V_k$ .

## B. MSLM Multienergetic System

The MSLM differs from the classical case in that the MCP is not a monoenergetic source of electrons. The electron current from a typical MCP has a continuous energy distribution  $n_o(V_k)$  ranging between zero and  $eV_m$ , where  $-V_m$  ( $V_m > 0$ ) is the MCP bias voltage. Here,  $n_o(V_k)dV_k$  is the number of MCP output electrons per unit area per unit time with energy between





independent of the polarization of the light (i.e.,  $\Delta\Phi = \Delta\Phi_x = \Delta\Phi_y$ ), and

$$\sigma_r = \epsilon_0 \lambda / 2n_0^2 r_{13} l_x, \quad (10)$$

where  $\lambda$  is the wavelength of the readout light,  $n_0$  is the ordinary refractive index of the crystal, and  $r_{13}$  the electrooptic coefficient of interest. For a 1-mm thick LiNbO<sub>3</sub> crystal,  $\sigma_r$  is approximately  $0.8 \times 10^{-7}$  C/cm<sup>2</sup> at 6328 Å.

The write and erase times are generally limited by the maximum MCP current available.

#### V. Exposure Sensitivity

The halfwave exposure  $S_r$  of the device is the write light energy per unit area that is required to change the phase of the readout light by  $\pi$  rad and is given, for both write modes, by

$$S_r = \int_0^{\pi} I_w(t) dt, \quad (11)$$

where  $t_r$  is given by either Eq. (8) or (9).

#### VI. Spatial Resolution

The spatial resolution of the MSLM is determined by the fidelity of the proximity focusing<sup>16</sup> and by the fringing of the electric fields in the electrooptic crystal. To maintain good proximity focusing, the longitudinal velocity component of the primary electrons must be much greater than the transverse component. This condition is achieved in the gridless device by setting  $V_b$  a few hundred volts above the desired voltage swing of the crystal. In devices employing an acceleration grid, the grid voltage  $V_a$ , which optimizes electron removal from the crystal, is generally enough to impart sufficient longitudinal kinetic energy to the primary electrons to maintain good proximity focusing.

The case of crystal-limited resolution, which applies to all MSLMs built so far, has been discussed at length by Roach<sup>17</sup> and generalized by Owechko and Tanguay.<sup>18</sup> For structures similar to the MSLM, Roach has shown that the crystal-limited resolution, as measured by the spatial bandwidth  $w_1$  (MTF roll-over frequency) is given by

$$w_1 = \frac{\epsilon_{\parallel}/l_x + \epsilon_g/l_g}{\pi[(\epsilon_{\parallel}\epsilon_{\perp})^{1/2} + \epsilon_g]}, \quad (12)$$

where  $l_g$  is the gap width,  $\epsilon_{\perp}$  is the dielectric constant perpendicular to the direction of the charge-induced electric field,  $\epsilon_g$  is the dielectric constant of the vacuum gap, and  $\epsilon_{\parallel}$  and  $l_x$  are as defined in Eq. (8).

From Eq. (12) it is clear that, in principle, the spatial bandwidth can be increased by reducing either the gap width  $l_g$  or the crystal thickness  $l_x$ . However, the product of the crystal-limited spatial bandwidth  $w_1$  and the low-frequency halfwave charge sensitivity  $S_r(0)$  of such devices is a constant which does not depend on device dimensions.<sup>17</sup> Thus, any improvement in spatial bandwidth will be at the expense of charge sensitivity. For the MSLM,  $S_r(0)$  is given by

$$S_r(0) = \left\{ \sigma_r \left[ 1 + \left( \frac{\epsilon_g}{\epsilon_{\parallel}} \right) \left( \frac{l_x}{l_g} \right) \right] \right\}^{-1}. \quad (13)$$

For convenience all MSLMs built so far have employed thick (0.5-mm) crystals and wide ( $\sim 0.5$ -mm)

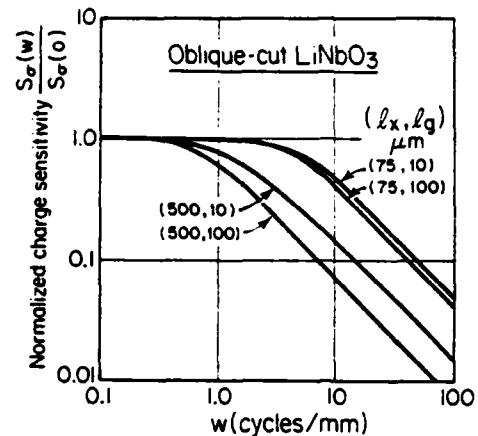


Fig. 6. Calculated normalized charge sensitivity  $S_r(w)/S_r(0)$  vs spatial frequency  $w$  for an oblique-cut LiNbO<sub>3</sub> MSLM with crystal thickness and gap width as parameters. The crystal cut is such that the normal to the surface makes an angle of 55° with the  $z$  axis and lies in the plane containing the  $z$  and  $-y$  axes.

gaps. Future LiNbO<sub>3</sub> and LiTaO<sub>3</sub> devices will employ crystals 75–250  $\mu$ m thick and gaps of  $\sim 100$ –500  $\mu$ m. A  $z$ -cut LiTaO<sub>3</sub> device with a 75- $\mu$ m thick crystal and a 100- $\mu$ m gap will have an MTF rollover of about 4.7 cycles/mm which corresponds to a spatial resolution of better than 10 cycles/mm at the 50% point on an MTF curve. The minimum crystal thickness is limited by dielectric breakdown and by the difficulties associated with polishing thin crystals; the minimum gap width must be large enough to prevent arcing during operation.

The MSLM can be further optimized for both intensity and phase modulation by employing a crystal cut that minimizes the halfwave surface charge density. For LiNbO<sub>3</sub>, this cut is such that the normal to the crystal surface lies in the plane containing the  $z$  and  $-y$  axes and makes an angle of 55° with the  $z$  axis.<sup>19</sup> With this cut, the electrically induced birefringence alters the polarization of the readout light, and the reflection halfwave voltage falls to a minimum value of  $\sim 1250$  V. Figure 6 shows how the calculated spatial resolution of such a device depends on crystal thickness and gap width.

#### VII. Storage

Stored charge images will diffuse with a characteristic relaxation time that depends on the finite surface and bulk conductivities of the crystal or the dielectric mirror. The device, therefore, must be framed through the write, read, and erase periods in a time that is much shorter than the charge relaxation time.

#### VIII. Prototype Devices

Two simple prototype devices have been built. The first is a vacuum demountable device employing a 25-mm diam MCP in proximity focus with a nominally plane-parallel 0.5-mm thick crystal that is coated on one side with a transparent electrode of indium tin oxide. Three  $z$ -cut crystals have been evaluated in this

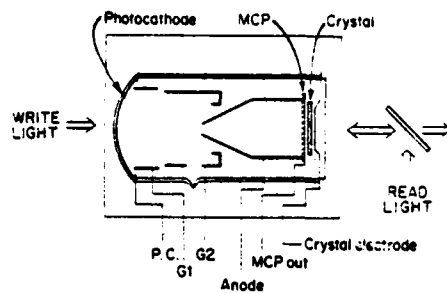


Fig. 7. Vacuum sealed, visible photocathode, prototype MSLM employing electron optics between the photocathode and the MCP and proximity focusing between the MCP and the crystal.

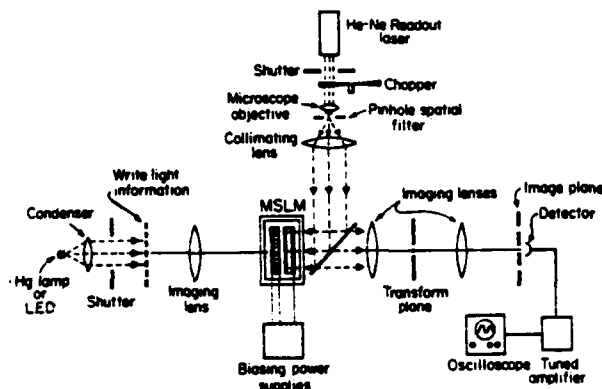


Fig. 8. Setup, with interferometric readout, used to measure the write and erase times, the spatial resolution, the image storage characteristics, and the operations achievable with the MSLM.

device: One  $\text{LiTaO}_3$  and one  $\text{LiNbO}_3$  crystal without dielectric mirrors, and one  $\text{LiNbO}_3$  crystal with dielectric mirrors on both sides (Fabry Perot configuration). In each case, the gap between the MCP and the crystal was 0.5 mm wide. A planar acceleration grid was sometimes inserted into the gap. The Inconel electrode on the input face of the MCP served as the photocathode. This device was activated with ultraviolet write light (254 nm) from a mercury lamp.

The second device is vacuum sealed and employs a visible alkali photocathode with 6% quantum efficiency at 655-nm wavelength. The gap in this device is 0.5 mm wide, and the electrooptic plate is a nominally plane-parallel 0.5-mm thick  $z$ -cut  $\text{LiTaO}_3$  crystal without a dielectric mirror. There is no grid in this device. To simplify fabrication, this device was built by modifying a Hamamatsu Corp. image intensifier tube. In this design, electron optics are used to image electrons from the photocathode onto the MCP, and proximity focusing is employed between the MCP and the crystal. The vacuum sealed, visible photocathode device is shown schematically in Fig. 7. An LED was used as the source of write light for this device.

The arrangement shown in Fig. 8 was used to measure the write and erase times, the spatial resolution, the image storage characteristics, and the image processing operations achievable with these devices. An interferometric readout scheme employing the Haidinger

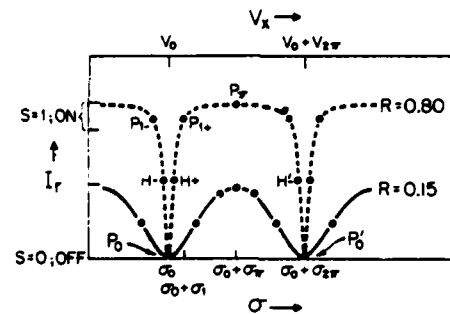


Fig. 9. Interferometric readout intensity characteristic for an uncoated  $\text{LiTaO}_3$  or  $\text{LiNbO}_3$  crystal ( $R = 0.15$ ) and for a Fabry-Perot ( $R = 0.80$ ) crystal.

interference patterns produced by multiple reflections between the front and back surfaces of the plane-parallel crystals was used. The surface reflectivity of uncoated  $\text{LiTaO}_3$  and  $\text{LiNbO}_3$  (0.15 at normal incidence) provided sufficient readout image contrast for experimental purposes (see Fig. 9).

The demountable  $\text{LiTaO}_3$  device without a dielectric mirror and with a grid in the gap was cycled at 20 frames/sec with full modulation depth and at 100 frames/sec with 20% modulation depth. The demountable Fabry Perot  $\text{LiNbO}_3$  device, employing an acceleration grid, was cycled at 40 frames/sec with full modulation depth, and up to 200 frames/sec with 20% modulation depth. The MCP in this device had a strip current of 20  $\mu\text{A}$  (at  $V_m = 1$  kV). MCP manufacturers are now developing MCPs with strip currents in excess of 100  $\mu\text{A}$  (at  $V_m = 1$  kV), so it is expected that the speed of the device can be increased by at least a factor of 5 in the near future.

The measured halfwave exposure of the visible photocathode device for the electron deposition write mode was 2.2  $\text{nJ}/\text{cm}^2$  at 655-nm wavelength, making it  $\sim 3$  orders of magnitude more sensitive than the other real-time, optically addressed spatial light modulators.<sup>4-6</sup> The gain of the MCP in this device was less than 1000. Therefore, with the standard MCP gain of  $10^4$ , the halfwave exposure of this device should be comparable to the calculated value of 0.3  $\text{nJ}/\text{cm}^2$ .<sup>1</sup>

With the visible photocathode  $\text{LiTaO}_3$  device, optical information storage times of up to two months with negligible charge diffusion have been observed. Because of the thick (0.5-mm) crystals and the wide ( $\sim 0.5$ -mm) gaps used in the prototype devices, their spatial resolution was only  $\sim 2$  cycles/mm at the 50% point on an MTF curve. However, as shown in Sec. VI, the resolution can be improved to  $\sim 10$  cycles/mm at the 50% point by employing 75 to 100  $\mu\text{m}$  thick crystals.

## IX. Achievable Image Processing Operations

By exploiting the secondary electron emission characteristics of the surface that stores the charge distribution, a variety of sophisticated image processing operations are possible. These include analog and digital intensity thresholding on stored images, edge enhancement, contrast enhancement, contrast reversal,



10 (A), (B) CONTRAST REVERSAL



11 (A), (B) IMAGE ADDITION



12 (A)-(C) IMAGE SUBTRACTION



13 (A)-(C) ANALOG AND DIGITAL THRESHOLDING



14 (A)-(C) CONTRAST ENHANCEMENT



15 (A), (B) AND OPERATION

Figs. 10-15. Some of the image processing operations achieved with the visible photocathode prototype MSLM.

image addition and subtraction, and binary-level logic operations such as AND, OR, EXCLUSIVE OR, and NOR. The binary (two-level irradiance) logic operations are best performed in a device employing a grid. The grid accelerates the MCP electrons and sets the maximum charge density level. Thus, any point on the crystal can be written to the full charge density without a loss of proximity focusing.

The MSLM interferometric readout intensity characteristic  $I_r$  as a function of crystal surface charge density  $\sigma$  is shown in Fig. 9. The solid curve is for an uncoated LiTaO<sub>3</sub> or LiNbO<sub>3</sub> crystal such as that used in the visible photocathode, prototype MSLM. The

reflectivity  $R$  of the uncoated surfaces of these crystals is  $\sim 0.15$ . The dashed curve is typical of a Fabry-Perot crystal with equal surface reflectivities. The point  $P_0$  is a null reflection point, and  $\sigma_0$  is the surface charge density required to bias the crystal at  $P_0$ . The points  $H+$  and  $H-$  are half-power points, and the points  $P_{1-}$  and  $P_{1+}$  are the 90% of peak transmission points. The point  $P_{\pi}$  is a peak transmission point with a corresponding crystal surface charge density of  $\sigma_0 + \sigma_{\pi}$ . Similar points can be identified on the  $R = 0.15$  characteristic. Notice the improved charge sensitivity for the off-to-on transition for a Fabry-Perot device.

All the image processing operations illustrated here were achieved with the vacuum sealed, visible photocathode, prototype MSLM using the arrangement shown in Fig. 8. The fine fringe pattern that modulates all the readout images in Figs. 10-15 is a result of interference caused by reflections from the contiguous surfaces of the MCP and the crystal. This pattern will disappear when crystals with dielectric mirrors are used.

#### A. Contrast Reversal

As was pointed out earlier, images can be written into the MSLM as either positive or negative charge distributions. And since both LiNbO<sub>3</sub> and LiTaO<sub>3</sub> exhibit the linear electrooptic effect, contrast reversed images can be written by reversing the polarity of the surface charge distribution. This is illustrated in Figs. 10(A) and (B) for a square input optical image written as a negative and a positive charge distribution, respectively, in the visible photocathode MSLM.

The operation of contrast reversal can, in principle, also be performed on stored images. If, for example, an image is stored along the path  $P_0P_{1+}$ , contrast reversal can be achieved either by adding a uniform electron distribution of  $\sigma_{H-} - \sigma_{H+}$  or by removing a uniform electron density of  $\sigma_{H+} - \sigma_{H-}$ . In practice it is easier to add than to remove large quantities of charge uniformly.

#### B. Image Addition and Subtraction

The addition of two images is best achieved by successively recording both images by the electron-deposition mode. Image addition with the visible photocathode MSLM is illustrated in Figs. 11(A) and (B) for a set of horizontal line sources [image  $A_1$ ] and a set of vertical line sources [image  $A_2$ ].

To implement image subtraction, the base line readout intensity of the MSLM is first set at a half-power point. This offset is necessary to ensure that all points of the result (after subtraction) are positive. If, for example, the base line half-power point  $H+$  is used, the first image  $A_1$  is written by secondary electron emission, and the second image  $A_2$  is written by electron deposition. The exposures of  $A_1$  and  $A_2$  must be controlled so that all parts of both images are written within the most linear part of the readout intensity characteristic. The operations leading to  $A_2 - A_1$  are illustrated in Figs. 12(A)-(C) for a horizontal bar image  $A_1$  which intersects a vertical bar image  $A_2$ .

### C. Analog Thresholding

Consider two areas  $A'$  and  $A''$  within an electron distribution on the surface of the crystal with electron densities  $\sigma'$  and  $\sigma''$ , respectively. If  $\sigma''$  is sufficiently greater than  $\sigma'$ , then  $V_b$  can be adjusted so that, when the photocathode is uniformly illuminated, primary electrons from the MCP are repelled from  $A''$  but not from  $A'$ . Under these conditions  $A'$  and all areas with electron density less than  $\sigma'$  will be erased, while  $A''$  and all other areas for which  $\sigma > \sigma''$  will be unaffected. This operation (analog level thresholding) corresponds to erasing all the parts of an image for which the intensity falls below some threshold intensity  $I_t$ . An example of analog thresholding is illustrated in Figs. 13(A) and (B).

Here analog thresholding is used to erase the lowest intensity level in a three-level image leaving the higher intensity levels unaffected.

Repeated applications of this operation (multiple-level thresholding) can be used to analyze the spatial distribution of intensities in an image. Analog thresholding is useful in the implementation of contrast enhancement and the logic operations AND and XOR.

### D. Stored Image Digital Thresholding (Hard Clipping)

In binary-level optical logic operations it is often desirable to digitize images by means of an operation in which all intensities below some chosen threshold level  $I_t$  are transformed to the same lower level (e.g.,  $S = 0$  in Fig. 9), and all those above  $I_t$  are restored to the same upper level (e.g.,  $S = 1$ ). This operation, also called hard clipping, can be achieved in a three-step process of which the first step is analog thresholding. In the second step, the photocathode is flooded uniformly with light and all the remaining nonzero intensities are transformed to the same saturation intensity level set by the grid voltage. Then analog thresholding is repeated to restore the lower level intensities to the  $S = 0$  state. Figure 13(C) illustrates the hard clipping result derived after the analog thresholding operation [Figs. 13(A) and (B)] on the three-level system.

### E. Real-Time Hard Clipping

This operation is most conveniently performed in the secondary emission write mode. The MSLM is initially biased in the OFF state with charge density  $\sigma_0$ . Then  $V_b$  is ramped downward (from higher to lower voltage) at a rate  $\dot{V}_b$  with the optical image incident on the photocathode. All the intensities below some threshold level  $I_t$  (which depends on  $\dot{V}_b$ ) will be barely recorded because, at their locations, electrons cannot be removed fast enough from the crystal to prevent the gap field from eventually repelling all future primary electrons. Thus, all intensities below threshold will remain at a low intensity level ( $S = 0$  state). Because the slope of the  $V_x$  vs  $I_w$  characteristic is known<sup>20</sup> to be very steep between threshold and saturation, virtually all write light intensities above threshold are written to the maximum charge density which is set to coincide with the  $S = 1$  state.

This operation can lead to real-time contrast enhancement if the crystal has a low halfwave voltage (e.g., DKDP at  $-51^\circ\text{C}$ ,  $V_\pi \approx 200$  V) and if  $\dot{V}_b$  is adjusted so that the spatial intensity variations of the image are mapped onto the knee of the  $V_x$  vs  $I_w$  curve.

### F. Contrast Enhancement

Contrast enhancement of stored images is a direct consequence of analog thresholding since in this operation the low-level intensities in an image can be reduced to an even lower level, leaving the high-level intensities unaffected. An example of contrast enhancement using level thresholding is illustrated in Figs. 14(A)–(C) with the visible photocathode MSLM. In Fig. 14(B) the stored image shown in Fig. 14(A) is washed out by the addition of a uniform charge density to the surface of the crystal. In Fig. 14(C) the contrast is enhanced by the level thresholding operation.

### G. Stored-Image Edge Enhancement

Suppose that a stored image of relatively uniform intensity was written with an average charge density level of  $\bar{\sigma}$  on a uniform background of charge density  $\sigma_0$ . Edge enhancement can be performed on this image by flooding the photocathode uniformly with light until the average charge density of the image reaches a level of  $\sigma_0 + \sigma_{2\pi}$  (OFF state), and then using analog thresholding to restore the background to the level  $\sigma_0$  (OFF state). Under these conditions, the charge density will fall abruptly from an average value of  $\sigma_0 + \sigma_{2\pi}$  inside to a value of  $\sigma_0$  outside the image. Thus, on the average the charge density at the edges of the image will be at a level of  $\sigma_0 + \sigma_\pi$  which corresponds to the ON state. That is, the edges of the image will be enhanced.

### H. Real-Time Edge Enhancement

With the modulator biased in the OFF state at  $P_0$  with a uniform charge density  $\sigma_0$ , real-time edge enhancement of an image of relatively uniform intensity can be achieved by writing the image, in the electron deposition mode, to an average level of  $\sigma_0 + \sigma_{2\pi}$  (OFF state). Again, the edges of the image will have an average charge density of  $\sigma_0 + \sigma_\pi$  (ON state) and, therefore, will be enhanced relative to the rest of the image. Notice that the modulator must be cycled through a full wave of phase modulation in order to implement this operation. Because of possible damage to the visible-photocathode prototype modulator we have not yet attempted this operation.

### I. OR Operation

The implementation of this operation depends on the type of device being used. Consider first a Fabry-Perot device with the high-reflectivity readout characteristic shown in Fig. 9. The base line charge density is first set at  $\sigma_0$  which corresponds to the  $S = 0$  state. If two binary-level images  $B_1$  and  $B_2$  are now each written one at a time with a charge density  $\sigma_1$ , the charge density at the intersection of images  $B_1$  and  $B_2$  will be  $\sigma_0 + 2\sigma_1$  (the  $S = 1$  state), whereas all the other parts of these images will have a charge density of  $\sigma_0 + \sigma_1$  (also the  $S$

= 1 state). The background will remain in the  $S = 0$  state with a charge density of  $\sigma_0$ . The result will be the OR operation.

If the device exhibits the low-reflectivity readout characteristic shown in Fig. 9, after images  $B_1$  and  $B_2$  are each written with a charge density of  $\sigma_\pi/2$ , digital thresholding must be performed to restore all parts of the composite image to a charge density of  $\sigma_0 + \sigma_\pi$  which corresponds to the  $S = 1$  state and all parts of the background to a charge density of  $\sigma_0$  which corresponds to the  $S = 0$  state.

#### J. AND Operation

This operation is implemented in the same way for both types of device. In each case the base line charge density is set at  $\sigma_0$  ( $S = 0$  state), and the two binary-level images  $B_1$  and  $B_2$  are written one at a time with a charge density of  $\sigma_\pi/2$ . Analog thresholding is then used to remove all electron densities that are less than or equal to  $\sigma_0 + \sigma_\pi/2$ ; the result will be the AND operation of  $B_1$  and  $B_2$ . The AND operation is illustrated in Figs. 15(A) and (B) with the visible photocathode MSLM for a horizontal pair of line sources [image  $B_1$ ] and a vertical pair of line sources [image  $B_2$ ].

#### K. EXCLUSIVE OR (XOR) Operation

This operation is implemented in the same way for both types of device. Starting with the modulator at  $P_0$  in the  $S = 0$  state with a uniform charge density  $\sigma_0$ , images  $B_1$  and  $B_2$  are written, one at a time, with a charge density of  $\sigma_\pi$ . The intersection of the two images will then be in the  $S = 0$  state at the point  $P_0$  with a charge density of  $\sigma_0 + \sigma_{2\pi}$ , whereas all the other parts of images  $B_1$  and  $B_2$  will remain in the  $S = 1$  state with a charge density of  $\sigma_0 + \sigma_\pi$ . The result will be the XOR operation.

#### L. NOR Operation

With the grid voltage set at  $V_0 + V_{2\pi}$ , the steps leading to the XOR operation are performed first. The photocathode is then uniformly flooded with light until all the parts of the composite image [ $B_1$  and  $B_2$ ] reach the maximum charge density of  $\sigma_0 + \sigma_{2\pi}$  which corresponds to the  $S = 0$  state. The background will then have a charge density of  $\sigma_0 + \sigma_\pi$  ( $S = 1$  state). Thus the NOR operation is achieved.

#### X. Comments

The spectral versatility, the high exposure sensitivity, the long storage times, and the wide variety of image processing operations that can be achieved by exploiting secondary electron emission are the most outstanding features of the MSLM. Since none of the characteristics of the present prototype devices is at its fundamental limit, it should be possible to improve all aspects of the performance of the MSLM.

Specifically, it should be possible to realize an exposure sensitivity of better than  $1 \text{ nJ/cm}^2$  in either a  $\text{LiTaO}_3$  or a  $\text{LiNbO}_3$  device by employing an MCP with the standard gain of  $10^4$ . Also, the present framing rate of 40 Hz (full modulation depth) can be improved even

further by (1) using a higher strip current micro-channel plate, and (2) coating the surface of the crystal with a material (such as  $\text{MgO}$ ) that has a very high secondary electron emission coefficient. Additionally, by reducing the crystal thickness to  $\sim 75 \mu\text{m}$ , the spatial resolution at the 50% point on an MTF curve should be  $\sim 10$  cycles/mm. For such thin crystals it will be necessary to employ the optimum crystal cut so that the operating voltages and, therefore, the probability of dielectric breakdown in the crystal can be significantly reduced.

Despite the low resolution of the visible photocathode prototype MSLM, it has been demonstrated that the MSLM is also capable of performing a wide variety of important signal processing operations in real time as well as on stored images. The accuracy, dynamic range, and linearity of these operations are currently being investigated. Alternative means of implementing logic operations with the MSLM are described in Ref. 20.

Several very inspiring discussions with Armand R. Tanguay, Jr., are gratefully acknowledged. The research is supported in part by the Air Force Office of Scientific Research under grant AFOSR-77-3328. Extensive use was made of the central facilities of the Center for Materials Science and Engineering, supported by the National Science Foundation under grant DMR-78-24185. A. M. Weiss is supported by a Fannie and John Hertz Foundation fellowship.

#### References

1. C. Warde, A. D. Fisher, D. M. Cocco, and M. Y. Burmawi, *Opt. Lett.* **3**, 196 (1978).
2. C. Warde and A. D. Fisher, *Proc. Soc. Photo-Opt. Instrum. Eng.* **177**, 67 (1979).
3. C. Warde, A. M. Weiss, and A. D. Fisher, *Proc. Soc. Photo-Opt. Instrum. Eng.* **218**, 59 (1980).
4. B. A. Horowitz and F. J. Corbett, *Opt. Eng.* **17**, 353 (1978).
5. D. Casasent, *Opt. Eng.* **17**, 365 (1978).
6. W. P. Bleha *et al.*, *Opt. Eng.* **17**, 371 (1978).
7. B. Leskovar, *Phys. Today* **30**, 42, No. 11, Nov. (1977).
8. J. L. Wisa, *Nucl. Instrum. Methods* **162**, 587 (1979).
9. *Applications for Microchannel Plates*, Varian Associates, Palo Alto, Calif.
10. P. J. Bjorkholm, L. P. VanSpeybroeck, and M. Hecht, *Proc. Soc. Photo-Opt. Instrum. Eng.* **108**, 189 (1977).
11. K. W. Dolan and J. Chang, *Proc. Soc. Photo-Opt. Instrum. Eng.* **106**, 178 (1977).
12. B. Kazan and M. Knoll, *Electronic Image Storage* (Academic, New York, 1968).
13. A. J. Guest, *Acta Electron.* **14**, 79 (1971).
14. A. M. Tyutikov and L. B. Tsoi, *Sov. J. Opt. Technol.* **43**, 86 (1976).
15. M. N. Devyatkov *et al.*, *Izv. Akad. Nauk SSSR Ser. Fiz.* **40**, 2604 (1976).
16. E. H. Eberhardt, *Appl. Opt.* **16**, 2127 (1977).
17. W. R. Roach, *IEEE Trans. Electron Devices* **ED-21**, 453 (1974).
18. Y. Owechko and A. R. Tanguay, Jr., *Proc. Soc. Photo-Opt. Instrum. Eng.* **218**, 67 (1980).
19. K. F. Hulme, *IEEE J. Quantum Electron.* **QE-7**, 236 (1971).
20. A. D. Fisher, "Techniques and Devices for High-Resolution Adaptive Optics," Ph.D. Thesis, Dept. of Electrical Engineering and Computer Science, MIT (exp. May 1981).

# Oblique-cut LiNbO<sub>3</sub> microchannel spatial light modulator

C. Warde and J. I. Thackara

Department of Electrical Engineering and Computer Science and the Center for Materials Science and Engineering, Massachusetts Institute of Technology, Cambridge, Massachusetts 02139

Received March 22, 1982

Significant improvements in the spatial resolution, framing speed, optical quality, and space-domain image-processing capabilities of the microchannel spatial light modulator have been realized by employing oblique-cut rather than z-cut LiNbO<sub>3</sub> crystals, high-strip-current (250-μA) microchannel plates, and an acceleration grid in the gap of the device. In particular, a prototype device employing a 330-μm-thick, optimum-cut (rotated 55° from the z axis) LiNbO<sub>3</sub> crystal exhibited a framing rate in excess of 30 Hz with full modulation depth and a spatial resolution of ~1.9 cycles/mm at 50% contrast (~10 cycles/mm at 10% contrast). Additionally, four-level to two-level intensity image conversion, contrast reversal, contrast enhancement, edge enhancement, and the binary-level operations AND, NAND, OR, NOR, XOR, and NXOR have been demonstrated by operating the device in its space-domain image-processing mode.

The microchannel spatial light modulator (MSLM) is a versatile, real-time optical signal- and image-processing device that exhibits high optical sensitivity and high framing speed. It consists of a photocathode and a microchannel plate (MCP) in proximity focus with an optional planar acceleration grid and an electro-optic crystal plate, as shown in Fig. 1. The electro-optic plate carries a high-resistivity dielectric mirror on one side and a transparent conducting electrode on the other.

In the electron-deposition write mode, incoherent or coherent write light incident upon the photocathode creates an electron image, which is amplified by the MCP and proximity focused onto the surface of the dielectric mirror. The resulting spatially varying electric field modulates the refractive index of the electro-optic plate. Thus the readout light, which makes a double pass through the crystal, is spatially phase or amplitude modulated, depending on the crystal cut and readout scheme (polarization or interferometric) employed.

The image is erased by appropriately adjusting the device voltages and flooding the photocathode with light so that electrons are removed from the mirror surface by secondary electron emission. Alternatively, the device can be operated in the reverse mode, in which a positive-charge image is written by secondary electron emission and erased by adding electrons to the crystal. For Pockels-effect crystals, this leads to contrast-reversed images. Further details of the principles of operation of the device can be found elsewhere.<sup>1</sup>

The results described in this Letter were achieved with a vacuum-dismountable MSLM employing an oblique-cut LiNbO<sub>3</sub> crystal plate 330 μm thick. The crystal was cut such that the normal to its surface was located in the plane containing the z and -y axes and made an angle θ of 55° with the z axis. This crystal cut optimizes the half-wave voltage and the half-wave surface-charge density in the longitudinal mode.<sup>2</sup>

For the general crystal cut with orientation θ, it can be shown that the voltage-induced phase retardations

along the induced dielectric axes (x' = x and y') in the transmission mode are given by

$$\begin{aligned}\Delta\phi_x(\theta, V) &= \frac{-\pi}{\lambda} V \eta_0^3 (r_{13} \cos \theta + r_{22} \sin \theta) \\ &= \frac{\pi}{\lambda} V \eta_0^3 r_x(\theta)\end{aligned}\quad (1)$$

and

$$\begin{aligned}\Delta\phi_y(\theta, V) &= \frac{-\pi}{\lambda} V \eta_e^3(\theta) [(r_{13} \cos \theta - r_{22} \sin \theta) \cos^2 \theta \\ &\quad + (r_{33} - 2r_{42}) \cos \theta \sin^2 \theta] \\ &= \frac{\pi}{\lambda} V \eta_e^3(\theta) r_y(\theta),\end{aligned}\quad (2)$$

where  $\eta_e(\theta)$  is the extraordinary refractive index for light propagation along z', the normal to the crystal surface, and polarized in the y' direction. It can be shown that  $\eta_e(\theta)$  is given by

$$\eta_e(\theta) = \frac{\eta_0 \eta_E}{(\eta_0^2 \sin^2 \theta + \eta_E^2 \cos^2 \theta)^{1/2}}. \quad (3)$$

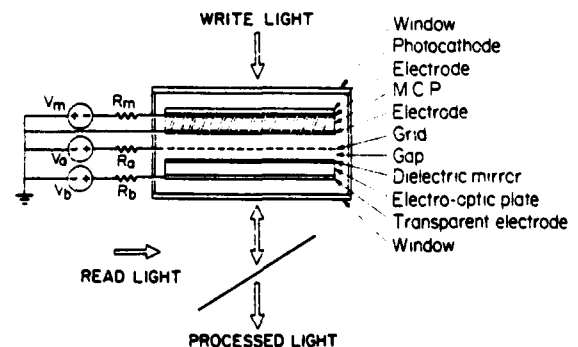


Fig. 1. The microchannel spatial light modulator.



In Eqs. (1)–(3),  $V$  is the applied voltage,  $\lambda$  is the wavelength of the light in *vacuo*,  $\eta_o$  and  $\eta_E$  are the ordinary refractive index and the principal value of the extraordinary refractive index, respectively, and  $r_{13}$ ,  $r_{22}$ ,  $r_{33}$ , and  $r_{42}$  are elements of the electro-optic tensor for LiNbO<sub>3</sub>.

The relative phase retardation  $\Gamma$  is given by  $\Gamma = \phi_y - \phi_x$ , and the corresponding transmission half-wave voltage  $V_{\pi T}$  is given by

$$V_{\pi T}(\theta) = \frac{\lambda}{\eta_e^3(\theta)r_y(\theta) - \eta_o^3r_x(\theta)}. \quad (4)$$

The values of the refractive indices and electro-optic coefficients for LiNbO<sub>3</sub> place the minimum value of  $V_{\pi T}$  near  $\theta = 55^\circ$ .

It is clear that, when this crystal is read out in coherent light between crossed polarizers (oriented at  $45^\circ$  to the  $x$  axis), the signal is modulated in both amplitude and phase. Amplitude-only modulation can be achieved by a sandwich of two appropriately oriented crystals of equal thickness. At 6328-Å wavelength, for  $\theta = 55^\circ$ , the calculated value of  $V_{\pi T}$  is 2300 V, compared with 6200 V ( $\Gamma = \phi_x = \phi_y = \pi$ ) for the  $z$ -cut material. For crystals operated in the reflex mode, such as those in the MSLM,  $V_{\pi R} = V_{\pi T}/2$ , and the half-wave surface-charge density  $\sigma_{\pi R}$  is given by  $\sigma_{\pi R} = \epsilon_0 \epsilon_1 V_{\pi R}/l_x$ , where  $\epsilon_0$  is the permittivity of free space and  $\epsilon_1$  is the dielectric constant for LiNbO<sub>3</sub> parallel to the  $z'$  axis. The measured half-wave value of  $V_{\pi R}$  for our samples was 1250 V. This corresponds to a calculated value of  $\sigma_{\pi R}$  of  $0.14 \mu\text{C}/\text{cm}^2$ .

The half-wave write time of the standard MSLM in the electron-deposition write mode is given by

$$t_{\pi w} = \sigma_{\pi R}/J_{pw}, \quad (5)$$

where  $J_{pw}$  is the primary-write current density incident upon the dielectric mirror. Note that  $J_{pw}$  will be less than the MCP output-current density  $J_0$  in devices employing an acceleration grid because the grid intercepts a portion of  $J_0$ . Thus  $J_{pw} < J_0 \ll I_s/A$ , where  $I_s$  and  $A$  are, respectively, the strip current and the active area of the MCP.

The corresponding half-wave erase time is given by<sup>1</sup>

$$t_{\pi e} = \frac{\sigma_{\pi R}}{J_g} = \frac{\sigma_{\pi R}}{J_{pe}} (\delta' - 1)^{-1}, \quad (6)$$

where the gap current  $J_g$  depends on the effective collected secondary electron-emission coefficient  $\delta'$  and  $J_{pe}$  is the primary-current density incident upon the dielectric mirror. The coefficient  $\delta'$  depends on the grid and mirror voltages, the energy distribution of the MCP output electrons, and the electronic properties of the dielectric mirror materials. Additionally,  $\delta'$  is often much smaller than  $\delta_{\max}$ , the peak value of the standard secondary electron-emission curve, which is measured on an uncharged surface with a gap field of 0 V/cm. Note that  $J_{pe} \leq J_{pw}$ . The inequality holds when the grid potential is greater than the surface potential of the dielectric mirror because the slightly repulsive field, which must be maintained in the gap during secondary-emission erasure, reduces the effective transmittance of the grid.

A vacuum-demountable device employing a 330- $\mu\text{m}$ -thick oblique-cut crystal was fabricated. This device employed a single dielectric-mirror coating on the crystal and was read out between crossed polarizers. The MCP used had a strip current of 250  $\mu\text{A}$  and a gain of  $1.1 \times 10^4$  at 1 kV of bias. The device was studied with and without an acceleration grid. The grid had a spatial frequency of 30 cycles/mm.

The strip-current-limited framing rate of the oblique-cut LiNbO<sub>3</sub> prototype device described above was 30 Hz at full modulation depth and 60 Hz at 50% modulation depth with the 250- $\mu\text{A}$  strip-current MCP. The corresponding half-wave write (electron-deposition) and erase times were 10 and 23 msec, respectively.

The normalized light-to-light coherent modulation transfer function (MTF) was experimentally determined by using a U.S. Air Force resolution test chart as the input image, measuring  $I_{\max}(\nu)$  and  $I_{\min}(\nu)$ , and substituting into the formula

$$\text{MTF}_l = \frac{1}{m} \frac{I_{\max}(\nu) - I_{\min}(\nu)}{I_{\max}(\nu) + I_{\min}(\nu)}. \quad (7)$$

Here  $I_{\max}(\nu)$  and  $I_{\min}(\nu)$ , respectively, stand for the maximum and minimum intensity values at spatial frequency  $\nu$  in the coherent readout beam and  $m$  is the spatial-modulation index of the input write light.

The measured normalized light-to-light coherent MTF of the standard oblique-cut LiNbO<sub>3</sub> prototype device was found to have a value of approximately 1.9 cycles/mm at 50% contrast for the 330- $\mu\text{m}$ -thick crystal, a gap of 500  $\mu\text{m}$ , and no grid. This is in good agreement with the calculated value of 2.0 cycles/mm at 50% contrast (10 cycles/mm at 10% contrast) assuming perfect transfer of the optical image on the photocathode to an electron image on the dielectric mirror. Similar results were obtained when the grid was inserted and the grid voltage was maintained above 2 kV.

By exploiting the secondary-electron-emission characteristics of the dielectric mirror and the charge-readout intensity characteristic of the crystal, several image-processing operations can be achieved by direct processing in the space domain (see Ref. 1). These include contrast reversal, contrast enhancement, edge enhancement, image addition and subtraction, and analog and digital intensity-level thresholding as well as binary-level logic operations, such as AND, NAND, OR, NOR, XOR, and NXOR.

Figure 2 shows some of the results of image processing in the space domain with the oblique-cut LiNbO<sub>3</sub> MSLM. Note the significant improvements in optical quality and spatial resolution over the earlier results of Ref. 1 with a 0.5-mm-thick  $z$ -cut LiTaO<sub>3</sub> crystal.

Figure 2(A) shows the imaging of a 1951 U.S. Air Force resolution chart. The sequence of Figs. 2(B)–2(D) illustrates analog and digital space-domain intensity thresholding. Figure 2(B) shows a four-level image. Figure 2(C) shows the same image after space-domain thresholding in which quadrant 1 was reduced to the zero-intensity level of quadrant 3, leaving quadrants 2 and 4 unchanged. Figure 2(D) is the resultant binary-level image after the MSLM with a stored image of Fig. 2(C) was illuminated uniformly



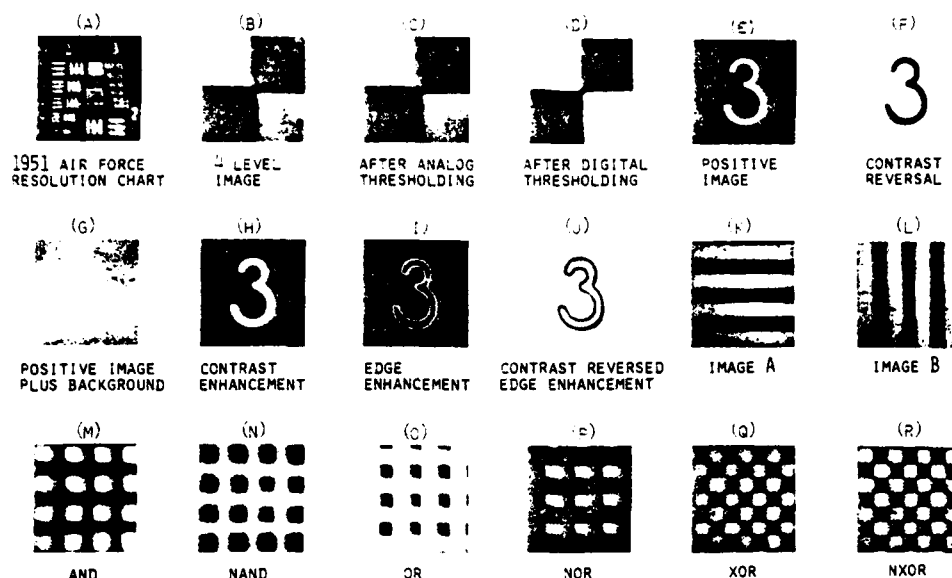


Fig. 2. Some of the image-processing operations achieved through space-domain processing with the oblique-cut  $\text{LiNbO}_3$  MSLM.

with light to bring quadrant 4 to the level of quadrant 2 and thresholding was again employed to restore quadrants 1 and 3 back to zero.

Figures 2(E) and 2(F) illustrate contrast reversal. In both cases the images were written by electron deposition. The crystal was first biased, by means of secondary electron emission, with a uniform positive-charge background at either a minimum in the transmittance characteristic [Fig. 2(E)] or at maximum transmittance [Fig. 2(F)].

Figures 2(G) and 2(H) illustrate contrast enhancement. In Fig. 2(G) the image shown in Fig. 2(E) was washed out with background illumination. Figure 2(H) shows the contrast-enhanced result after analog thresholding. Figures 2(I) and 2(J) illustrate edge enhancement of a binary-level image. Figure 2(I) results from Fig. 2(e) when the write-image exposure corresponds to the full-wave surface-charge density  $\sigma_{2\pi}$ ; similarly, Fig. 2(J) results from Fig. 2(F) for the full-wave input-image exposure.

Figures 2(M)–2(R) illustrate the AND, NAND, OR, NOR, XOR, and NXOR operations of the horizontal and vertical bar images shown in Figs. 2(K) and 2(L).

All the images shown in Fig. 2 were achieved by direct image processing in the space domain using the non-linear-readout intensity characteristic of the crystal in conjunction with the secondary-electron-emission characteristics of the dielectric mirror. Except for Figs. 2(O) and 2(P), all the images were achieved in a device without an acceleration grid.

Several of the significant advantages of oblique-cut  $\text{LiNbO}_3$  over z-cut  $\text{LiNbO}_3$  and  $\text{LiTaO}_3$  for intensity modulation have been demonstrated in this Letter. The polarization-readout scheme used with the oblique-cut  $\text{LiNbO}_3$  crystal leads to a more uniform optical field across the crystal than does the interferometric-readout technique that was used earlier with the z-cut material. The half-wave voltage of the oblique-cut material is reduced by a factor of 2.4 over that of the z-cut material, and this translates into a corresponding increase in optical sensitivity and framing speed.

However, for phase-only modulation, the z-cut material may be preferred over the  $55^\circ$ -cut material for some applications involving very-low-level unpolarized readout light since it would not be necessary to polarize the readout beam for processing with the z-cut material.

This research was supported in part by the U.S. Air Force Office of Scientific Research under grant AFOSR-77-3328. Extensive use was made of the central facilities of the Center for Materials Science and Engineering, supported by the National Science Foundation under grant DMR-78-24185.

## References

1. C. Warde, A. M. Weiss, A. D. Fisher, and J. I. Thackara, *Appl. Opt.* **20**, 2066 (1981).
2. K. F. Hulme, P. H. Davies, and V. M. Cound, *J. Phys. C* **2**, 855 (1969).

# APPENDIX III

## Simple closed-loop system for real-time optical phase measurement

Arthur D. Fisher and Cardinal Warde

Department of Electrical Engineering and Computer Science and Center for Materials Science and Engineering, Massachusetts Institute of Technology, Cambridge, Massachusetts 02139

Received January 2, 1979

A simple closed-loop system for estimating optical phase, called an interference phase loop, is presented. In this system the output intensity from an elementary interferometric phase sensor (e.g., Zernike phase contrast, homodyne, heterodyne, polarization, or shearing interferometer) is detected and used to drive a phase modulator in the path of the wavefront being measured. It is shown theoretically and experimentally that with large gain this configuration ignores amplitude fluctuations and unambiguously estimates phase at high speed over a dynamic range of multiple- $\pi$  radians. When self-interference (e.g., Zernike phase contrast) is employed, monochromatic light is not required.

Real-time measurement of optical phase fluctuations  $\phi_i(x,y,t)$  is required for such diverse applications as studying refractive-index variations in plasmas or gases, visualizing transparent structures, measuring the atmospheric phase distortion to be compensated for in an adaptive optical system, and extracting phase information from a coherent optical data processor. Elementary phase visualization techniques, such as Zernike phase contrast, heterodyne, homodyne, shearing, and polarization interferometry, suffer from a limited and nonlinear dynamic range of  $\pi$  radians as well as from  $2\pi$  and phase-quadrant ambiguities in the inferred phase. In addition, they do not by themselves distinguish wavefront-amplitude variations from phase variations. A variety of quite sophisticated electrical and optical systems has been designed to overcome these difficulties and accurately estimate phase.<sup>1-5</sup>

This Letter presents a simple closed-loop phase-estimation system (Fig. 1) called an interference phase loop (IPL), in which the output from one of the elementary interferometers mentioned above is used to drive a phase modulator in the path of the wavefront being measured. The spatially parallel drive signal to the modulator is shown to be the phase estimate. In many cases the interferometer intensity itself (e.g., at C in Fig. 1) also becomes an intensity representation of  $\phi_i(x,y,t)$ , the phase to be measured. It is shown both theoretically and experimentally that, with large system gain, this basic feedback configuration can inherently ignore amplitude fluctuations, eliminate phase-quadrant ambiguities, and continuously estimate phase over multiple- $\pi$  radians of dynamic range. When self-interference is employed (e.g., shearing or polarization interferometry or Zernike phase contrast), monochromatic light is not required.

A phase-measurement system employing an ac interferometer with feedback from a phase modulator in its local oscillator (LO) beam was previously reported.<sup>5</sup> However, instead of exploiting the inherent properties of optical phase feedback, which we present here, that

system employed complicated analog and digital electronics. Additionally, the IPL does not use an LO beam in the self-interference implementations.

Similar principles are also implicit in adaptive-optical, transmitter-predistortion systems with feedback derived from a target reflection [e.g., coherent optical adaptive techniques (COAT)<sup>1</sup> or Cathey *et al.*<sup>6</sup>] and closed-loop adaptive receivers.<sup>1,7</sup> However, most of these systems employ heterodyne or synchronous detection and more-complex electronics to separate the phase from amplitude variations. The IPL is also somewhat related to a recently reported closed-loop bistable Fabry-Perot.<sup>8</sup>

The homodyne-heterodyne implementation will be analyzed; the analysis is similar for self-interference. In Fig. 1 the modulator adds a constant phase shift  $\phi_0(x,y)$  and an electrically controlled phase  $\phi_m(x,y,t)$  to the input wave. The modulated beam is assumed to suffer an attenuation  $\alpha$  and phase shift  $\phi_1(x,y)$  in traveling from the modulator to the detector. When the spatial dependence is suppressed, LO field  $E_l$  and modulator field  $E_m$  combine to produce the intensity:

$$I = I_0 + I_1 \cos[\phi_i - (\phi_m + \phi_0) - (\phi_1 + \pi/2) - \phi_1 - (\omega_i - \omega_l)t], \quad (1a)$$

where

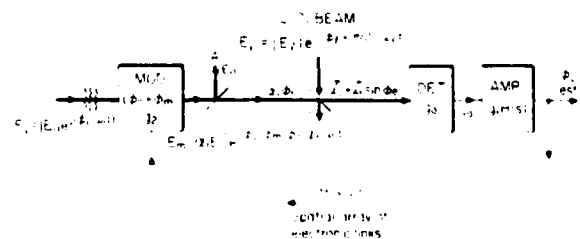


Fig. 1. Homodyne-heterodyne implementation of the IPL. MOD is a spatial phase modulator. DET is a detector array. AMP is an amplifier array.  $E_m$  and  $E_l$  are defined at the detector face.

$$I_0 = \alpha^2 |E_i|^2 + |E_t|^2 \quad (1b)$$

and

$$I_1 = 2\alpha |E_i| |E_l|. \quad (1c)$$

**This is more conveniently expressed as**

$$I = I_0 + I_1 \sin \phi_e. \quad (2a)$$

**Here**

$$\phi_e = \phi_i - \phi_m - \phi_b \quad (2b)$$

is the loop phase error, with  $\phi_b = \phi_0 + \phi_1 + (\omega_i - \omega_l)t$ .

The detector in Fig. 1 can be modeled as exhibiting threshold and saturation by

$$i_0 = \begin{cases} 0 & I \leq I_t \\ g_0(I - I_t) & I_t \leq I \leq I_s \\ g_0(I_s - I_t) & I \geq I_s \end{cases} \quad (3)$$

The phase modulator is also assumed to have a limited dynamic range; assuming that  $0 \leq \phi_m \leq \phi_s$ ,

$$\phi_m = \begin{cases} 0 & i_1 \leq 0 \\ g_2 i_1 & 0 \leq i_1 \leq \phi_s/g_2. \\ \phi_s & i_1 \geq \phi_s/g_2 \end{cases} \quad (4)$$

The frequency response of the detector and modulator can be lumped into the amplifier transfer function  $H(s)$ ; thus, in the Laplace domain,

$$\mathbf{I}_1(s) = g_1 H(s) \mathbf{I}_0(s). \quad (5)$$

**Combining Eqs. (2)–(5) results in an implicit expression for the modulator phase in its linear operating region:**

$$\Phi_m(s) = g_0 g_1 g_2 H(s) (I_0 - I_t + I_1 \sin \Phi_e). \quad (6)$$

Introducing the new lumped variables  $G_0$  and  $G_1$  and using Eq. (2b),

$$\Phi_m = H(s)[G_0 + G_1 \sin(\Phi_i - \Phi_m - \Phi_h)]. \quad (7)$$

In order to proceed, a single-pole loop filter,  $H(s) = \lambda/(s + \lambda)$ , will be assumed; infinite-bandwidth ( $\lambda \rightarrow \infty$ ) or integrating [ $H(s) = 1/s$ ] filters can be viewed as special subcases. Owing to system nonlinearities, it is easier to analyze the loop's operation in the time domain. With the single-pole filter and Laplace transform pair  $s \leftrightarrow d/dt$ , Eq. (7) results in the equation

$$\dot{\phi}_m = \lambda[-\phi_m + G_0 - G_1 \sin(\phi_m - \phi_i + \phi_b)], \quad (8)$$

where  $\dot{\phi}_m = d\phi_m/dt$ .

Graphical techniques<sup>9</sup> provide a powerful tool for studying these transcendental differential equations, particularly with such complications as saturation and threshold. The modulator state-space plot ( $\phi_m$  versus  $\phi_m$ ) of Fig. 2(a) is a graphical representation of Eq. (8). Static background phase ( $\phi_b = 0$ , i.e., homodyne or self-interference) is assumed, making it convenient to reference the input phase to  $\phi_b$ ; i.e.,  $\phi_i \equiv \phi_i - \phi_b$  ( $\phi_i \equiv 0$  when  $\phi_i = \phi_b$ ). Limited modulator dynamic range ( $0 \leq \phi_m \leq \phi_s$ ) and detector threshold and saturation are also assumed. Whenever the derivative is positive ( $\phi_m > 0$ ) the modulator phase increases, following a traiec-

tory to the right in Fig. 2(a); whenever  $\dot{\phi}_m < 0$  the trajectory goes to the left. Stable equilibria (circled points) occur where the trajectories converge from above and below onto the  $\dot{\phi}_m = 0$  axis.

According to Eq. (8), the whole sinusoidal trajectory of Fig. 2(a) shifts laterally in proportion to  $\phi_i$ . The stable equilibrium points of  $\phi_m$  thus follow the trajectories in Fig. 2(b), continuously tracking  $\phi_i$  variations within the system bandwidth ( $\phi_i < \lambda\phi_i$ ). These equilibrium trajectories can also be seen by setting  $\dot{\phi}_m = 0$  in Eq. (8); it then follows that

$$\phi_i' = \phi_m + 2n\pi + \sin^{-1}[(G_0 - \phi_m)/G_1]. \quad (9)$$

Thus, with large gain ( $G_1 \rightarrow \infty$ ), the modulator phase estimates the input phase:  $\phi_m \approx \phi_i' + 2n\pi$ .

As  $\phi_i$  increases,  $\phi_m$  eventually saturates; then  $\phi_m = \phi_s$  and  $\phi_m = 0$  until an unstable equilibrium of Fig. 2(a) reaches  $\phi_s$ . From there the system follows the trajectory, which causes  $\phi_m$  to jump to the next-lowest stable equilibrium point. Similarly, with decreasing phase,  $\phi_m$  does not stay pinned at its minimum value but eventually returns to its phase-tracking region [Fig. 2(b)].

In practice there need not be a  $2n\pi$  degeneracy in  $\phi_m$ , since the value of the modulator phase before the system is turned on determines which equilibrium point in Fig. 2(a), and hence which trajectory in Fig. 2(b), is followed. For example, if a uniform calibrated intensity is occasionally shined into the detector to reset  $\phi_m$  at  $2\pi$ , then all the points in the wavefront will be operating on the  $\phi_m = \phi_i + 2\pi$  trajectory of Fig. 2(b).

Wavefront-amplitude fluctuations cause the offset  $G_0$  and gain  $G_1$  to vary. Variations in  $G_0$  cause the trajectories in Fig. 2(a) to shift up and down between the threshold and saturation limits; with large gain, only small perturbations in the equilibrium value of  $\phi_m$  result. Provided the gain  $G_1$  remains large, amplitude-induced fluctuations in gain are also inconsequential; only the error, which is already very small, will vary.

Notice that the interferometer intensity is both an unamplified version of the phase estimate [Fig. 1 with  $H(s) \approx 1$ ] and a representation of  $\phi_e$  [Eq. (2)]. Thus,

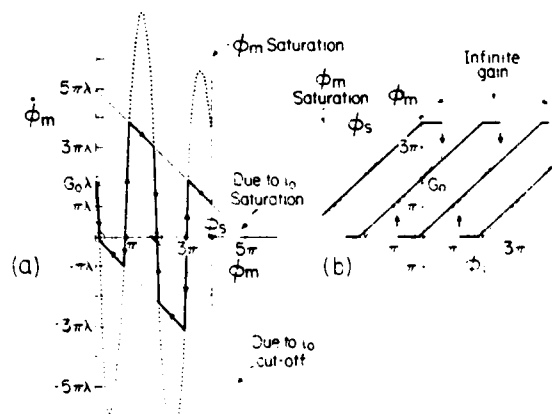


**Fig. 2.** (a) Modulator state-space trajectory ( $\dot{\phi}_m$  versus  $\phi_m$ ) from  $\dot{\phi}_m = \lambda[-\phi_m + G_0 - G_1 \sin(\phi_m - \phi_i)]$  with  $\phi_i = 0$ ,  $G_0 = 1.8\pi$ ,  $G_1 = 7.3\pi$ , and  $\phi_s = 3.8\pi$ . Stable equilibria are circled. (b) Phase estimation performance ( $\phi_m$  versus  $\phi_i$ ).

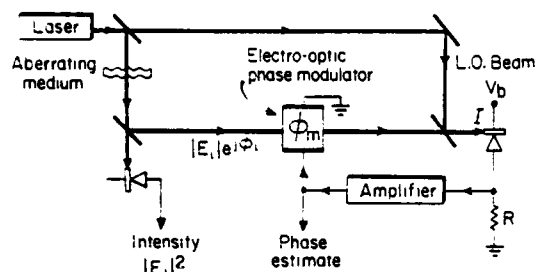


Fig. 3. Single-spatial-element homodyne IPL implemented with a Mach-Zehnder interferometer and with direct electrical readout of intensity  $|E_i(t)|^2$  and phase  $\phi_i(t)$ .

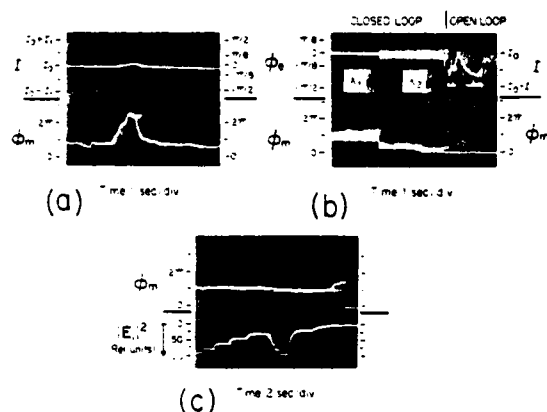


Fig. 4. Experimental results:  $I$  is interferometer intensity.  $\phi_e$  is derived from Eq. (2b).  $\phi_m$  is the modulator phase, i.e., the phase estimate of  $\phi_i$ . (a) Phase tracking ( $G_1 \approx 10\pi$ ). (b) Closed-loop and open-loop response to wideband (0–150-Hz) phase fluctuations with  $G_1 \approx 20\pi$  and two different loop-filter bandwidths ( $\lambda_1 \approx 10^4 \text{ sec}^{-1}$ ,  $\lambda_2 \approx 50 \text{ sec}^{-1}$ ). (c) Immunity to amplitude  $|E_i|$  fluctuations ( $G_1 \approx 20\pi$ ).

in analogy with a classical type-zero control system, the error,  $\sin \phi_e$ , is amplified to drive the output,  $\phi_m$ . It can also be shown that the input phase range corresponding to the full interferometer intensity range of  $2I_1$  [Eq. (2)] is extended from  $\pi$  radians in the elementary interferometer to  $2G_1 + \pi$  radians in the IPL system. The phase image (e.g., signal at C in Fig. 1) could be recorded with high-contrast film or a detector array having threshold and gain.

This analysis has been extended to include the heterodyne implementation, other loop filters [e.g.,  $H(s) = 1, K/S$ , or  $K'/(s + \lambda_1)(s + \lambda_2)$ ], and the system transient response. The IPL system is much like an electronic phase-lock loop,<sup>9</sup> particularly in the heterodyne implementation.

The single-element homodyne IPL system of Fig. 3 was constructed. A silicon photodiode and a transverse LiNbO<sub>3</sub> phase modulator were employed. The modulator had a half-wave voltage of 200 V and a breakdown voltage  $> 100 \text{ kV}$ ; however, the maximum amplifier voltage (700 V) limited the modulation to  $3.5\pi$  rad. The system had a dominant single pole, which was adjustable from 4 to 4000 Hz. With a high-breakdown-voltage ( $> 400 \text{ V}$ ) photodiode, it should be possible to

simplify the system further by eliminating the amplifier.

Figure 4(a) demonstrates the phase-tracking behavior of the phase estimate  $\phi_m$  (i.e., modulator voltage) and the interferometer intensity  $I$  (i.e., detector signal  $i_0$ ) for large phase variations produced by tilting a glass plate. The phase corresponding to a given tilt was calibrated by opening the loop and interpreting the nonlinear output of the resulting unmodified Mach-Zehnder interferometer. Figure 4(b) displays IPL operation in the presence of broadband (0–150-Hz) phase fluctuations. Notice that with large bandwidth and high gain all the fluctuations are tracked by  $\phi_m$  and “compensated” out of  $I$ . Compensation occurs because, with large gain, only a small change in  $I$  is required to drive a large change in  $\phi_m$ . In Fig. 4(c) an electro-optic amplitude-only modulator varied  $|E_i|$ ; note that the phase estimate  $\phi_m$  is insensitive to intensity variations of more than an order of magnitude.

Besides phase measurement, the IPL system is well suited for other applications. For example, the bistable (or multistable) operating characteristic of Fig. 2(b) could be exploited to construct a two-dimensional optical digital-processing element. In addition, Fig. 1 can be viewed as an adaptive optical system to compensate for atmospherically induced phase distortions,  $\phi_i(x, y, t)$ . With high gain the wavefront of  $E_0$  at A in Fig. 1 has phase  $\phi_b(x, y)$ , which is a system constant and can be made plane or any other desirable shape. The configuration of Fig. 1 can also generate the wavefront conjugate of  $\phi_i(x, y)$  in a second laser beam injected at A. An IPL system with 19 discrete hard-wired elements and a high-resolution “all-optical” version, employing a monolithic optically driven spatial phase modulator,<sup>10</sup> are under construction and will be presented in a future paper.

The authors wish to acknowledge helpful discussions with J. H. Shapiro. This research was supported by NSF grant ENG-74-00131 and by MIT's Center for Materials Science and Engineering under NSF grant DMR-76-80895.

## References

1. J. W. Hardy, Proc. IEEE 66, 651 (1978).
2. M. J. Lavan, G. E. Van Damme, and W. K. Cadwallende, Opt. Eng. 15, 464 (1976).
3. R. A. Sprague and B. J. Thompson, Appl. Opt. 11, 1469 (1972).
4. Y. Ichioka and M. Inuiya, Appl. Opt. 11, 1507 (1972).
5. G. W. Johnson and D. T. Moore, Proc. Soc. Photo-Opt. Instrum. Eng. 103, 76 (1977).
6. W. T. Cathey, C. L. Hayes, W. C. Davis, and V. F. Pizzurro, Appl. Opt. 9, 701 (1970).
7. G. Q. McDowell, D.Sc. thesis (MIT, Cambridge, Mass., 1971).
8. P. W. Smith and E. H. Turner, Appl. Phys. Lett. 30, 280 (1977).
9. A. J. Viterbi, Principles of Coherent Communications (McGraw-Hill, New York, 1966).
10. C. Warde, A. D. Fisher, D. M. Cocco, and M. Y. Burmawi, Opt. Lett. 3, 196 (1978).

# Technique for real-time high-resolution adaptive phase compensation

A. D. Fisher\* and C. Warde

Department of Electrical Engineering and Computer Science, Massachusetts Institute of Technology, Cambridge, Massachusetts 02139

Received March 16, 1983

An "all-optical" approach for the realization of adaptive optical systems potentially containing in excess of a million spatial-resolution elements is reported. A phase-measurement and -compensation technique called an interference phase loop is employed in conjunction with a monolithic optically addressed spatial light modulator (SLM). Wave-front phase compensation and shaping, and the ability to ignore amplitude fluctuations and compensate phase in real time over multiple  $\pi$  radians of dynamic range, were demonstrated in two discrete-channel laboratory test systems containing one and nineteen resolution elements. All-optical phase compensation with a monolithic SLM was also successfully demonstrated.

High-resolution adaptive optical systems, containing thousands to millions of spatial-resolution elements, offer the potential of considerably improving performance in such applications as<sup>1-3</sup> optical communications through low-visibility or turbulent atmospheric conditions, imaging through the atmosphere, and high-energy laser propagation. Most previous<sup>2</sup> adaptive optical systems consisted of arrays of individual phase estimators hard-wired to discrete modulators, a technology that cannot practically be extended to the required high resolutions. Instead, an all-optical parallel processing approach is presented here.

Figure 1 is a conceptual diagram of an all-optical phase-compensated communications receiver. The distorted received wave front passes through an *optically addressed* monolithic spatial phase modulator, which adds the appropriate phase to present a compensated, approximately planar wave front to the communications receiver. Part of the compensated wave front is fed back to a phase estimator whose output is an *optical* intensity proportional to the phase of the compensated beam. This *optical* control signal drives the spatial light modulator.

It should be stressed that, unlike the system presented here, high-resolution nonlinear (e.g., degenerate four-wave mixing) compensation schemes<sup>4</sup> generally require a double pass through the distorting medium. For example, a probe beam must initially be sent from the receiver to the transmitter, or a probe-beam glint must be received off the object in imaging applications.

Most existing<sup>3</sup> techniques for phase measurement appear to have undesirable performance limitations or seem too complicated for implementation in the all-optical phase estimator of Fig. 1. For example, elementary interferometers based on schlieren, heterodyne, or homodyne techniques are all-optical. However, without additional signal processing they cannot distinguish wave-front phase from amplitude variations, and they suffer from a nonlinear dynamic range of  $\pi$  radians as well as from  $2n\pi$  and phase-quadrant ambiguities. However, in an earlier Letter<sup>5</sup> we showed

that closed-loop configurations similar to Fig. 1 inherently simplify phase measurement. More specifically, it was demonstrated that a particular technique, termed an interference phase loop (IPL), wherein the output intensity from an elementary interferometer is fed back to drive a *phase-only* modulator in the path of the wave front being measured, overcomes the above-mentioned phase-measurement problems. Figure 1 becomes an example of an IPL when the phase estimator is an elementary interferometer.

Figure 2 illustrates a specific "all-optical" implementation of the IPL employing a homodyne interferometer and a reflection-readout monolithic phase modulator, a microchannel spatial light modulator (MSLM).<sup>6,7</sup> In the MSLM the electron image from the photocathode is amplified by the microchannel array plate and proximity focused onto the dielectric mirror. The spatially varying electric field induced by the charge distribution modifies the refractive index of the electro-optic crystal (e.g., LiNbO<sub>3</sub>), which phase modulates the reflected readout beam. A half-wave exposure sensitivity of 2.2 nJ/cm<sup>2</sup> ( $\lambda = 655$  nm), a framing rate of 30 Hz, and a spatial resolution of 10 line pairs per millimeter (lp/mm) (10% modulation transfer function) have been achieved with current MSLM's.<sup>7</sup> Quantum-limited sensitivity, kilohertz framing rates, mul-

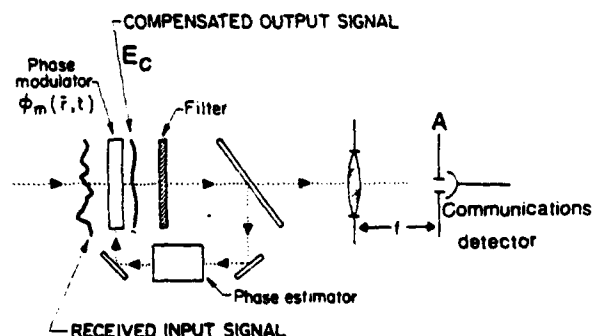


Fig. 1. All-optical adaptive phase-compensated communications (direct-detection) receiver.

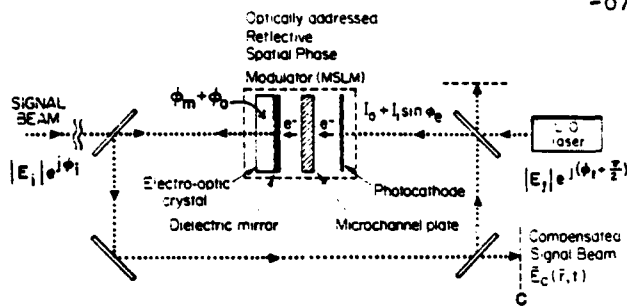


Fig. 2. An "all-optical" high-resolution IPL.

multiple  $2\pi$  phase modulation, and spatial resolution approaching 20 lp/mm are ultimately expected. The writing- and reading-light wavelengths can range from the IR through the UV, depending on the particular choice of photocathode and electro-optic crystal.

Theoretical and experimental studies have shown<sup>3,5</sup> that the IPL not only largely ignores amplitude fluctuations but also has no phase-quadrant ambiguity and can continuously estimate phase over multiple  $\pi$  radians of dynamic range. When schlieren interferometry is employed, monochromatic light is not required. In operation, the modulator phase and the elementary interferometer output intensity become representations of the phase estimate. With large loop gain, the phase error of the modulated beam (e.g.,  $E_c$  in Figs. 1 and 2) can be made arbitrarily small.<sup>3,5</sup> Hence the IPL also simultaneously achieves phase compensation.

The IPL can also be employed for wave-front conjugation<sup>3,5</sup> (e.g., by injecting a laser beam at C in Fig. 2) and high-resolution bistability/multistability.<sup>3,5</sup> In many respects, the IPL can be considered an optical phased-locked loop that directly tracks optical wave-front phase. It is also somewhat related to bistable optical devices incorporating feedback from a detector<sup>8,9</sup> and to a reported phase-measurement system that employed an ac interferometer with feedback by means of a phase modulator in its local oscillator beam.<sup>10</sup> Similar principles are also implicit in some closed-loop adaptive receivers<sup>2,11</sup> and some adaptive optical, transmitter-predistortion systems with feedback derived from a target reflection.<sup>2,12</sup>

Only the most basic operational principles of the homodyne interferometer implementation of the IPL are presented here. A more detailed discussion, which includes heterodyne and schlieren implementations, can be found elsewhere.<sup>3</sup>

In Fig. 2, the modulator adds a constant phase  $\phi_o(x, y)$  and an electrically controlled phase  $\phi_m(x, y, t)$  to the input corrupted wave. When the spatial and temporal dependencies are suppressed, the modulated and local-oscillator (LO) beams combine at the photocathode to produce the intensity

$$I = I_o + I_1 \sin \phi_e, \quad (1)$$

where

$$\phi_e = \phi_i - \phi_m - \phi_o - \phi_l \equiv \phi_i' - \phi_m. \quad (2)$$

Here  $I_o = |E_i|^2 + |E_l|^2$ ,  $I_1 = 2|E_i||E_l|$ ,  $\phi_i' \equiv \phi_i - (\phi_o + \phi_l)$ , and  $\phi_o + \phi_l$  is a static reference phase of the system (i.e.,  $\phi_i' = 0$  when  $\phi_i = \phi_o + \phi_l$ ).

The modulator phase,  $\phi_m$  in Fig. 2, is generally proportional to the write-beam intensity, with some temporal response. For example, with a single-pole low-pass time response, the dynamic behavior of the modulator is described by<sup>3,5</sup>

$$(d\phi_m/dt) + \omega_o \phi_m = \omega_o [G_o + G_1 \sin(\phi_i' - \phi_m)]. \quad (3)$$

Here  $G_o \equiv g(I_o - I_t)$ ,  $G_1 \equiv gI_1$ ,  $g$  is an electronic gain factor, and  $I_t$  is a detector threshold intensity. Typically,  $-2\pi \leq G_o \leq 2\pi$  and  $2\pi \leq G_1 \leq 50\pi$ .<sup>3</sup>

This nonlinear system has been shown<sup>3,5</sup> to be unconditionally stable, with equilibria ( $d\phi_m/dt = 0$ ) oc-

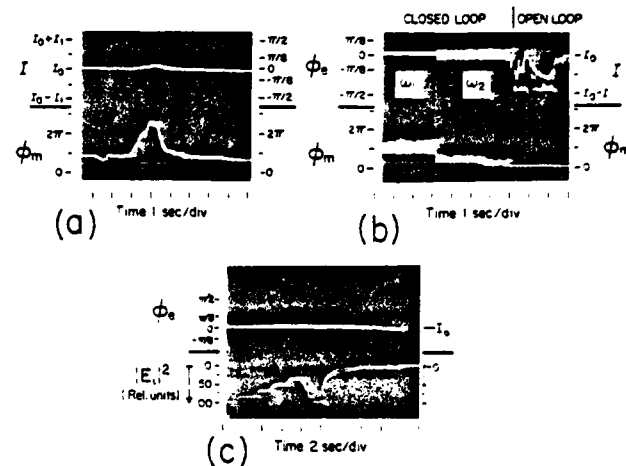


Fig. 3. Single-channel IPL experimental results. (a) Phase compensation ( $\phi_e \approx \text{constant}$ ) and simultaneous phase estimation ( $\phi_m \approx \phi_i'$ ),  $G_1 = 10\pi$ . (b) Closed-loop and open-loop response to 0-150-Hz-bandwidth input phase fluctuations with two different IPL loop-filter bandwidths ( $\omega_1 = 10^4 \text{ sec}^{-1}$  and  $\omega_2 = 50 \text{ sec}^{-1}$ ),  $G_1 = 20\pi$ . (c) Immunity of phase compensation ( $\phi_e \approx \text{constant}$ ) to amplitude  $|E_i|$  fluctuations,  $G_1 = 20\pi$ .

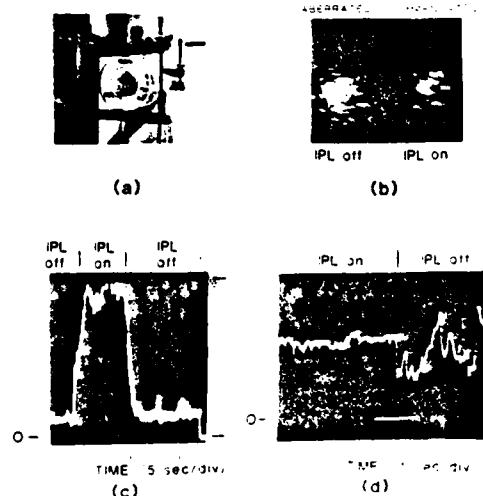


Fig. 4. Nineteen-element IPL experiments. (a) Nineteen-element discrete-channel modulator array. (b) Photographs of Fourier transforms of aberrated and compensated waves. (c), (d) Response of a diffraction-limited detector in the Fourier plane to (c) static and (d) dynamic phase fluctuations. (c) is the zero-light level.

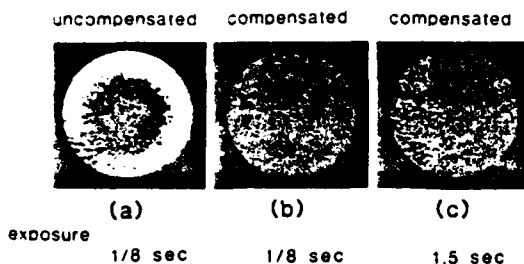


Fig. 5. Phase-compensation results with the "all-optical" MSLM/IPL system. (a) Interferogram of the initial phase distortion (dynamic range of  $\approx \pi$  rad). (b) Interferogram after IPL compensation. (c) Long-term exposure of (b) to show residual error. The fine fringes in the lower left of (a) and (c) are due to light that reflected from the MCP.

curing at  $\phi_m = \phi_i' - \sin^{-1}[(\phi_m - G_o)/G_1] + 2n\pi$ . Thus, with large gain,  $G_1 \gg |G_o - \phi_m|$ , the modulator phase estimates the input phase; i.e.,

$$\phi_m \approx \phi_i' + 2n\pi. \quad (4)$$

The  $n$  value generally remains constant, permitting continuous phase tracking over multiple  $\pi$  radians.<sup>3,5</sup> (In appropriate applications, however, the system can be made to exhibit multistability.) As long as  $G_1 \gg |\phi_m - G_o|$ , fluctuations in  $|E_i|$  and  $|E_l|$  have a negligible effect on  $\phi_m$  and  $\phi_e$ .<sup>3,5</sup>

The phase of the compensated signal beam (e.g.,  $E_c$  in Fig. 2) is  $\phi_c \equiv \phi_i - \phi_m - \phi_o = \phi_e + \phi_l$ . With large  $G_1$ ,  $\phi_e \approx 0$  and  $\phi_c \approx \phi_l$ . The IPL thus compensates  $\phi_c$  to the shape of the LO wave front, which can be designed to be planar. Note that the intrinsic modulator distortions  $\phi_o$  are removed from  $\phi_c$ .

An all-optical phase compensator similar to that shown in Fig. 2 was experimentally demonstrated. Since the resolution elements of a homodyne IPL are spatially decoupled, two discrete-channel laboratory systems containing one and nineteen resolution elements were also built to investigate IPL operation in greater depth.

Homodyne IPL performance was demonstrated previously in a single-channel system that employed a Si photodiode to drive a transverse LiNbO<sub>3</sub> modulator.<sup>5</sup> Figure 3(a) illustrates phase compensation. The error phase of the compensated beam,  $\phi_e$  ( $\phi_e = \phi_i' - \phi_m$ , represented by the interferometer intensity  $I$ ) remains relatively constant while  $\phi_m$  tracks  $>2\pi$  variation in  $\phi_i'$  produced by tilting a glass plate in the input beam. Figure 3(b) displays IPL operation with 0–150-Hz-bandwidth phase fluctuations. Notice that with large bandwidth and high gain all the fluctuations are compensated out of  $\phi_i'$  ( $\phi_e \approx \text{constant}$ ) and tracked by  $\phi_m$ . In Fig. 3(c),  $\phi_e$  exhibits insensitivity to intensity  $|E_i|^2$  variations of more than an order of magnitude.

The 19-element test system employed 19 Si photodiodes driving a hexagonal array of 19 reflective electrodes deposited on a disk of LiNbO<sub>3</sub>, as pictured in Fig. 4(a). Images of the Fourier transforms (at the equivalent of plane A in Fig. 1) of corrupted and IPL-compensated wave fronts are compared in Fig. 4(b). The compensated transform contains a sixfold symmetric pattern of repeating transforms that is due to sampling of the wave front by the hexagonal modulator array.

Figures 4(c) and 4(d), which display the intensity seen by a diffraction-limited detector in the Fourier plane (proportional to the Strehl ratio), illustrate compensation (IPL on) of mostly static (distorted Plexiglas and slight turbulence) and dynamic (heated-air) wave-front aberrations, respectively. The compensated Strehl ratio in Fig. 4(c) is increased by a factor of 7 to approximately the Strehl ratio of the unaberrated wave front.

Figure 5 shows a low-resolution demonstration of phase compensation with an "all-optical" MSLM-IPL system similar to that of Fig. 2. The initial uncompensated phase distortion, which had a dynamic range of about  $\pi$  radians, is depicted in Fig. 5(a). Figures 5(b) and 5(c) display the IPL-compensated interferogram. The long exposure of Fig. 5(c) reveals a very small residual phase error ( $\sim \lambda/20$ ). Unfortunately, the particular prototype MSLM that was employed had defects that prevented its use on high-resolution spatial phase aberrations. Recently improved MSLM's, however, should permit truly high-resolution MSLM-IPL phase compensation to be realized in the near future.

In conclusion, a versatile wave-front-compensation technique has been demonstrated that potentially offers the resolution as well as the speed and sensitivity required for a variety of adaptive phase-compensation applications. The ultimate performance of this technique will be determined by the characteristics of optically addressed spatial phase modulators, which are continually improving. An MSLM-based IPL is projected ultimately to be capable of compensating close to  $10^6$  (20 lp/mm over a 5-cm-aperture) coherence cells<sup>3</sup> of a highly corrupted wave-front fluctuating at kilohertz rates.

This research was supported in part under U.S. Air Force contract AFOSR-77-3328 and National Science Foundation grant ENG-78-21603. Use was made of the central facilities of the MIT Center for Materials Science and Engineering, which is supported under National Science Foundation grant DMR-78-24185.

\* Present address, Naval Research Laboratory, Washington, D.C. 20375.

## References

1. J. H. Shapiro and C. Warde, *Opt. Eng.* 20, 1 (1981).
2. J. W. Hardy, *Proc. IEEE* 66, 651 (1978).
3. A. D. Fisher, Ph.D. Thesis (Massachusetts Institute of Technology, Cambridge, Mass., 1981).
4. T. R. O'Meara, *Opt. Eng.* 21, 231 (1982).
5. A. D. Fisher and C. Warde, *Opt. Lett.* 4, 131 (1979).
6. C. Warde, A. M. Weiss, A. D. Fisher, and J. I. Thackara, *Appl. Opt.* 20, 2066 (1981).
7. C. Warde and J. I. Thackara, *Opt. Lett.* 7, 344 (1982).
8. P. W. Smith and E. H. Turne, *Appl. Phys. Lett.* 30, 280 (1977).
9. E. Garmire, J. H. Marburger, and S. D. Allen, *Appl. Phys. Lett.* 32, 320 (1978).
10. G. W. Johnson and D. T. Moore, *Proc. Soc. Photo-Opt. Instrum. Eng.* 103, 76 (1977).
11. G. Q. McDowell, D.Sc. Thesis (Massachusetts Institute of Technology, Cambridge, Mass., 1971).
12. W. T. Cathey, C. L. Hayes, W. C. Davis, and V. F. Pizzurro, *Appl. Opt.* 9, 701 (1970).

**END**

**FILMED**

**1-84**

**DTIC**